Supplement of Geosci. Model Dev., 18, 9119–9147, 2025 https://doi.org/10.5194/gmd-18-9119-2025-supplement © Author(s) 2025. CC BY 4.0 License.





Supplement of

Enhancing simulations of snowpack properties in land surface models with the Soil, Vegetation and Snow scheme v2.0 (SVS2)

Vincent Vionnet et al.

Correspondence to: Vincent Vionnet (vincent.vionnet@ec.gc.ca)

The copyright of individual parts of the supplement might differ from the article licence.

Supplement

S1 Additional model description

S1.1 Surface tiling and vegetation

10

S1.1.1 Land surface tiles and vegetation characteristics

SVS2 computes separated surface energy budgets for 6 land surface tiles that can co-exist within a grid cell: (i) exposed snow-free bare ground (bg), (ii) snow-free low vegetation (lv), (iii) snowpack on bare ground and low vegetation (sno), (iv) high vegetation (hv), (v) ground below high vegetation (ghv) and (vi) snowpack below high vegetation (snhv). SVS2 makes the distinction between the fraction of each tile i seen from space, $f_{s,i}$, and the fraction of each tile i seen from the underlying ground, $f_{g,i}$. The fraction $f_{s,*}$ affects surface/atmosphere heat and mass exchanges while the fraction $f_{g,*}$ affects surface/soil heat and mass exchanges. An overview of each tile and the corresponding fraction is given in Table S1.

SVS2 uses the same default vegetation classification as SVS1 (Husain et al., 2016; Alavi et al., 2016) and considers 22 vegetation types as described in Table S2. Within a grid cell, the areal fraction A of each vegetation type is derived from land cover databases such as the global European Space Agency Climate Change Initiative Land Cover database (ESA-CCILC, https://www.esa-landcover-cci.org/) or the North American Land Change Monitoring System (NALCMS, http://www.cec. org/north-american-land-change-monitoring-system/). Each vegetation type is classified as low (L) or high vegetation (H) and is associated with a vegetation-type dependent coverage c_{veg} . For a given vegetation type, c_{veg} represents the fraction

Table S1. Summary of SVS2 land surface tiles and respective fractions seen from the atmosphere and from the ground. C_H , C_L and C_B represents the fractional coverage of the land surface tile by high vegetation, low vegetation and bare ground. p_{sno} and p_{snhv} represent the fractions of the ground covered by snow in open terrain and below high vegetation. SVF is the sky view factor through high vegetation.

| Index | Land surface tile | Fraction seen from the atmosphere | Fraction seen from the ground |
|-------|--------------------------------------|-----------------------------------|-------------------------------|
| bg | Exposed snow-free bare ground | $C_B(1-p_{sno})$ | $C_B(1-p_{sno})$ |
| lv | Snow-free low vegetation | $C_L(1-p_{sno})$ | $C_L(1-p_{sno})$ |
| sno | Snowpack on bare ground and low veg. | $(1-C_H)p_{sno}$ | $(1-C_H)p_{sno}$ |
| hv | High vegetation | $C_H(1-SVF)$ | 0 |
| ghv | Ground below high veg. | $C_HSVF(1-p_{snhv})$ | $C_H(1-p_{snhv})$ |
| snhv | Snowpack below high veg. | C_HSVFp_{snhv} | $C_H p_{snhv}$ |

covered by actual vegetation while the rest is covered by bare ground. An annual cycle of c_{veg} is considered for certain vegetation types, such as crops (Tab. S2). For forest types, the vegetation coverage is set to 0.99 and the forest density, V_{dens} , is computed using an external database as described in Sect. S1.1.2. In the absence of snow, the fractional coverage of the land surface tile by high vegetation, low vegetation and bare ground are computed as: $C_H = \sum_{i,H} A_i c_{veg,i}$, $C_L = \sum_{i,L} A_i c_{veg,i}$ and $C_B = 1 - C_H - C_L$. The sky view factor through high vegetation v depends on forest density (V_{dens}) and the average vegetation area index (V_{AI}) of trees composing high vegetation as described in Section 2.3.1 of the main manuscript.

In SVS2, the fractions of different land surface tiles seen from the atmosphere and from the ground are affected by the presence of snow as detailed in Tab. S1. They depend on the snow cover fractions in open terrain (p_{sno}) and in forested environments (p_{snhv}) . p_{sno} and p_{snhv} are defined as in Brun et al. (2013) and Boone et al. (2017):

25
$$p_{sno} = \min(1., W_{sno}/W_{crit})$$
 (S1)

$$p_{snhv} = \min\left(W_{snhv}/W_{crit}\right) \tag{S2}$$

where W_{sno} and W_{snhv} are total snow water equivalent in open terrain and below high vegetation (kg m⁻²), respectively, and W_{crit} is a critical value set to 1 kg m⁻². This low value for W_{crit} leads to a fully covered open terrain and/or ground below high vegetation as soon as snow is present. This approach is used in SVS2 to avoid unrealistic soil–snow conduction heat flux due to the unrealistic assumption of an identical soil physical state between the fractions that are covered by snow and those that are not (Monteiro et al., 2024). Such approach is not suitable for two-way coupling with an atmospheric model. Therefore, it will be revised in the future to include two separate soil columns within a grid cell (one below open terrain and one below forested terrain).

The aggregated surface energy balance for low and high vegetation (Sect S1.2.3, and Sect. 2.3 of the main manuscript) requires averaged values of vegetation properties, such as albedo, emissivity, V_{AI} . For a given property P, the average values for low (P_L) , and high vegetation (P_H) are computed as $P_L = 1/C_L \times \sum_{i,L} A_i P_i$ and $P_H = 1/C_H \times \sum_{i,H} A_i P_i$ where P_i is the property for each vegetation type (Table. S2).

Table S2. Vegetation type in SVS2 and corresponding characteristics. H and L refer to high and low vegetation, respectively, "cycle" refers to vegetation characteristics with an annual cycle, specified on a monthly basis. V_{AI} is the vegetation area index of the elements composing the vegetation (including leaves, stem and branches).

| Vegetation type | H/L | c_{veg} (i) | Albedo (-) | Emissivity (-) | V_{AI} (-) |
|----------------------------|-----|---------------|------------|----------------|--------------|
| evergreen needleleaf trees | Н | 0.99 | 0.14 | 0.996 | 4 |
| evergreen broadleaf trees | Н | 0.99 | 0.12 | 0.996 | 6 |
| deciduous needleleaf trees | Н | 0.99 | 0.14 | 0.990 | cycle |
| deciduous broadleaf trees | Н | 0.99 | 0.18 | 0.990 | cycle |
| tropical broadleaf trees | Н | 0.99 | 0.13 | 0.996 | 6 |
| drought deciduous trees | Н | 0.99 | 0.17 | 0.990 | 4 |
| evergreen broadleaf shrub | L | 0.50 | 0.14 | 0.954 | 3 |
| deciduous shrubs | L | 0.50 | 0.18 | 0.954 | cycle |
| thorn shrubs | L | 0.50 | 0.19 | 0.954 | 3 |
| short grass | L | 0.70 | 0.20 | 0.993 | 1 |
| long grass | L | 0.30 | 0.19 | 0.993 | cycle |
| crops | L | cycle | 0.20 | 0.981 | cycle |
| rice | L | cycle | 0.21 | 0.981 | cycle |
| sugar | L | cycle | 0.18 | 0.981 | cycle |
| maize | L | cycle | 0.18 | 0.981 | cycle |
| cotton | L | cycle | 0.25 | 0.981 | cycle |
| irrigated crops | L | 0.85 | 0.18 | 0.981 | 1 |
| tundra | L | 0.50 | 0.17 | 0.992 | cycle |
| swamp | L | 0.60 | 0.12 | 0.995 | 4 |
| desert | L | 0.00 | 0.30 | 0.941 | 0 |
| mixed wood forests | Н | 0.99 | 0.15 | 0.993 | cycle |
| mixed shrubs | Н | 0.99 | 0.15 | 0.993 | cycle |

S1.1.2 Density of high vegetation

The density of high vegetation in SVS2, V_{dens} , is read as input. In the simulations/tests described in this paper, the density is derived from the Global Tree Cover dataset (Hansen et al., 2013) at 30-m grid resolution. This dataset represents the estimated maximum tree canopy cover per pixel in the range 1-100%. The 30-m dataset is then averaged at the simulation resolution of SVS2 by the processor of geophysical fields used in the GEM atmospheric model. 30-m pixels that are classified as water, cities, ice, bare ground and low vegetation according to the Global Land Cover and Land Use at 30-m resolution (Hansen et al., 2022) are excluded from the averaging process to obtain an averaged value that only is representative of the 30-m forested pixels present within a given SVS2 grid cell.

S1.1.3 Height of Arctic vegetation

To run SVS2 in the Arctic with parameterizations of Royer et al. (2021) and Woolley et al. (2024) that affect the density of basal snow, a map of distributed height of Arctic vegetation has been developed. It is based on the Circumpolar Arctic Vegetation Map (CAVM Raynolds et al., 2019) at 1-km resolution. CAVM is a comprehensive mapping project that documents and classifies vegetation across the entire Arctic region. In CAVM, the Arctic is defined as the area of the Earth with tundra vegetation, an arctic climate and arctic flora, with the tree line defining the southern limit (Raynolds et al., 2019). To obtain a value of vegetation height for each CAVM vegetation type over North America and Greenland, rasters of retrieved height of Arctic vegetation at 20-m resolution from Bartsch et al. (2020) over several areas in Alaska and Yukon have been upscaled to the CAVM resolution (1 km). Then, the 1-km maps of vegetation height have been combined with the CAVM vegetation types over the areas considered by Bartsch et al. (2020) to determine a mean vegetation height for each vegetation type in CAVM. Finally, these mean vegetation heights have been applied to corresponding vegetation classifications over the whole CAVM domain, generating a map of the height of Arctic vegetation above the tree line. A value of 0 cm was used for the CAVM category B1, that represents dry to wet barren landscapes with very sparse plant cover. A value of 5 cm was used for the CAVM categories B2a, B2b and B3 covering partially vegetated (dwarf shrubs, lichen, or alpine vegetation) barren areas. Figure S1 shows heights of Arctic vegetation for the Canadian Arctic, Alaska and Greenland. The height of Arctic vegetation is only defined above the treeline where the CAVM is available. Vegetation height decreases from 30-40 cm just north of the treeline where shrubs are abundant to 0 cm in the polar desert, in the north of the Canadian Arctic and Greenland.

S1.2 Surface energy budget

The surface energy balance for the two snow-related tiles is simulated by the detailed snowpack model Crocus as described in the main article (Sect. 2.2). Simulation of the surface energy balance for high vegetation (taking into account intercepted snow and liquid water) is also described in the main article (Sect. 2.3). The following subsections describe the computation of the surface energy balance for the remaining land surface tiles. They rely on the same approach and use a skin temperature that forms the interface between the soil and the atmosphere as in the ECLand scheme (Boussetta et al., 2021).

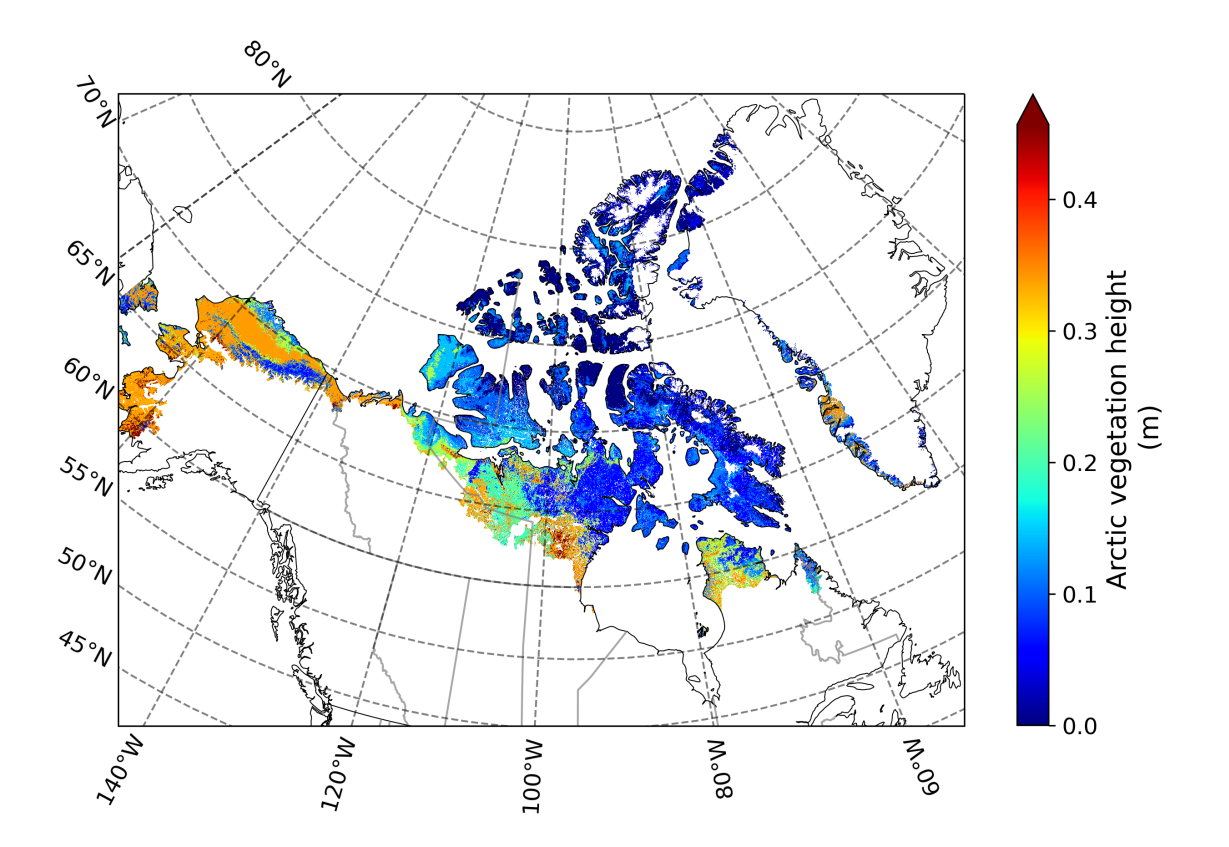


Figure S1. Map of Arctic vegetation height (m) at 1-km resolution over the Canadian Arctic, Alaska and Greenland.

70 S1.2.1 Exposed bare ground

The energy balance equation for the surface temperature of exposed bare ground is as follows:

$$R_{n,bq} - H_{bq} - LE_{bq} = \Lambda_{sk,bq} (T_{s,bq} - T_{soil,1})$$
 (S3)

where bg denotes the exposed bare ground, $R_{n,bg}$ the net radiation fluxes (W m⁻²), $T_{soil,1}$ is the temperature of the upper soil layer (K), H_{bg} and LE_{bg} are the sensible heat flux and latent heat flux towards the atmosphere (W m⁻²), respectively, and $\Lambda_{sk,bg}$ the skin conductivity for the exposed bare ground (W m⁻² K⁻¹). The net radiation over bare ground is given as:

$$R_{n,bq} = (1 - \alpha_{bq})SW + \epsilon_{bq} \left(LW - \sigma T_{s,bq}^4\right) \tag{S4}$$

where SW and LW are the incoming shortwave and longwave fluxes (W m⁻²), respectively, α_{bg} is the bare ground albedo (-) and ϵ_{bg} is the bare ground emissivity (-). They are determined as in the SVS1 land surface scheme (Husain et al., 2016) and

rely on a bilinear interpolation between the albedo and emissivity values of four "extreme" soil types—dry sand, wet sand, dry clay, and wet clay. They are computed as:

$$\alpha_{bg} = \alpha_{dry\,sand}A(1 - S_{WI}) + \alpha_{dry\,clay}(1 - A)(1 - S_{WI}) + \alpha_{wet\,sand}AS_{WI} + \alpha_{wet\,clay}(1 - A)S_{WI} \tag{S5}$$

$$\epsilon_{bg} = \epsilon_{dry\,sand} A (1 - S_{WI}) + \epsilon_{dry\,clay} (1 - A)(1 - S_{WI}) + \epsilon_{wet\,sand} A S_{WI} + \epsilon_{wet\,clay} (1 - A) S_{WI} \tag{S6}$$

in which $A = f_{sand}/(f_{sand} + f_{clay})$ denotes the soil texture ratio that depends on the fraction of sand and clay $(f_{sand} \text{ and } f_{clay}, \text{ respectively})$ and $S_{WI} = (w_1 - w_{1,wilt})/(w_{1,sat} - w_{1,wilt})$ is the soil wetness index of the near-surface soil layer, with w_1 being the soil moisture content for the first soil layer (m³ m⁻³). The properties that characterize the extreme soil types are obtained from Sumner (1999). The parameters $w_{1,wilt}$ and $w_{1,sat}$ are the soil water content at wilting point and at saturation (m³ m⁻³), respectively, for the first soil layer. Their calculation is described in Sect. S1.3.3.

The sensible heat flux over bare ground follows the same definition as in the SVS1 scheme (Husain et al., 2016):

90
$$H_{bg} = \frac{\rho_a c_p (T_{s,bg} - T_a)}{R_{a,bg}}$$
 (S7)

where ρ_a (kg m⁻³) and T_a (K) correspond to air density and temperature at the forcing atmospheric level, respectively, c_p is the specific heat of dry air (J K⁻¹ kg⁻¹), and $R_{a,bg}$ is the aerodynamical surface resistance of bare ground (s m⁻¹) given by $(C_{H,bg}V_a)^{-1}$ where $C_{H,bg}$ is the turbulent exchange coefficient for heat over bare ground (-) and V_a is wind speed at the forcing atmospheric level (m s⁻¹). $C_{H,bg}$ is computed by the surface turbulent scheme of the GEM model (Beljaars and Holtslag, 1991; Delage and Girard, 1992).

The latent heat of evaporation from bare ground follows SVS1 (Husain et al., 2016) and is written as $LE_{bg} = \rho_a L_{eff} E_{bg}$ where E_{bg} is bare ground water vapor flux and L_{eff} is effective latent heat (J kg⁻¹). Effective latent heat is computed to account for sublimation of ice in the soil, and is defined as follows:

$$L_{eff} = f_{ice}L_i + (1 - f_{ice})L_v \tag{S8}$$

in which $f_{ice} = w_{i,1}/(w_{i,1} + w_1)$ is the fraction of ice in the surface soil layer $(w_{i,1}$ is the volumetric solid water content of the upper soil layer, m³ m⁻³), and L_i and L_v are latent heat of sublimation and evaporation, respectively (J kg⁻¹). The bare ground vapor flux, E_{bg} (kg m⁻² s⁻¹), follows the formulation for bare ground evaporation which is implemented in SVS1 (Husain et al., 2016):

$$E_{bg} = \frac{\rho_a \left[H R_{bg} q_{sat} \left(T_{s,bg} \right) - q_a \right]}{R_{a,bg}} \tag{S9}$$

where HR_g is a "relative humidity" of bare ground (-), $q_{sat}(T_{s,bg})$ is saturated specific humidity of air near bare ground (kg kg⁻¹) at temperature $T_{s,bg}$ (K), and q_a is atmospheric specific humidity at the forcing atmospheric level (kg kg⁻¹). If the bare ground vapor flux is negative because low level air is more moist i.e., $q_a > q_{sat}(T_{s,bg})$, then E_{bg} is set to zero. The relative

humidity HR_{bq} of the bare ground surface is related to the first layer soil moisture w_1 following:

$$HR_{bg} = \begin{cases} \frac{1}{2} \left[1.0 - \cos\left(\frac{w_1}{w_{1,fc}}\pi\right) \right] & \text{if } w_1 < w_{1,fc} \\ 1 & \text{if } w_1 \ge w_{1,fc} \end{cases}$$
(S10)

where $w_{1,fc}$ is volumetric water content at the field capacity of the upper soil layer (Noilhan and Planton, 1989). It can be seen in Eq. S10 that when soil is very humid, it is assumed that the humidity of the bare ground surface is equivalent to a saturated surface (similar to a water surface). In case of dew flux when $q_a < q_{sat}(T_{s,bg})$, HR_{bg} is also set to 1.0 as in Husain et al. (2016).

The skin conductivity of exposed bare ground, $\Lambda_{sk,bg}$ (W m⁻² K⁻¹), provides the thermal connection between the skin level and the upper soil layer (Boussetta et al., 2021). It is computed as $\Lambda_{sk,bg} = 2\lambda_1/\Delta_{z_1}$ where Δ_{z_1} is the thickness of the upper soil layer (m) and λ_1 the thermal conductivity of the upper soil layer (W m⁻¹ K⁻¹, Eq. S20).

S1.2.2 Bare ground below high vegetation

The energy balance equation for the surface temperature of bare ground below high vegetation follows the same equation as for exposed bare ground (Eq. S3):

120
$$R_{n,qhv} - H_{ghv} - LE_{ghv} = \Lambda_{sk,qhv} (T_{s,qhv} - T_{soil,1})$$
 (S11)

where ghv denotes bare ground below high vegetation, $R_{n,ghv}$ net radiation fluxes (W m⁻²), $T_{soil,1}$ is the temperature of the upper soil layer (K), H_{ghv} and LE_{ghv} are the sensible heat flux and latent heat flux towards the atmosphere (W m⁻²), respectively, and $\Lambda_{sk,ghv}$ the skin conductivity for bare ground below high vegetation (W m⁻² K⁻¹). Net radiation over bare ground below high vegetation follows the same equation as for bare ground (Eq. S4) and for shortwave and longwave radiation uses values modified by the presence of high vegetation (Eq. 31 and 32 in the main manuscript). Turbulent fluxes of sensible and latent heat above bare ground below high vegetation are computed using air temperature and specific humidity taken at the reference forcing level above the canopy as in Koivusalo and Kokkonen (2002) and Gouttevin et al. (2015). The effect of canopy on the turbulent heat fluxes is accounted for in the computation of aerodynamic resistance between ground below the canopy and the reference forcing level above the canopy (Eq. 22 in the main manuscript). The skin conductivity of bare ground below high vegetation, $\Lambda_{sk,ghv}$, is computed as for the exposed bare ground: $\Lambda_{sk,ghv} = 2\lambda_1/\Delta_{z_1}$ where Δ_{z_1} is the thickness of the upper soil layer and λ_1 the thermal conductivity of the upper soil layer (Eq. S20). A future version of SVS2 will consider the effect of low vegetation and forest litter below the canopy (e.g., Napoly et al., 2017).

S1.2.3 Low vegetation

125

The energy balance equation for the surface temperature of snow-free low vegetation is as follows:

135
$$R_{q,lv} - H_{lv} - LE_{lv} = \Lambda_{sk,lv} (T_{s,lv} - T_{soil.1})$$
 (S12)

where lv denotes snow-free low vegetation, $R_{g,lv}$ the net radiation fluxes (W m⁻²), $T_{soil,1}$ is the temperature of the upper soil layer (K), H_{lv} the sensible heat flux (W m⁻²), and LE_{lv} the latent heat flux (W m⁻²), and $\Lambda_{sk,lv}$ the skin conductivity for low vegetation (W m⁻² K⁻¹). Net radiation over low vegetation is computed as in SVS1 (Husain et al., 2016):

$$R_{g,lv} = (1 - \alpha_{lv})SW + \epsilon_{lv} \left(LW - \sigma T_{s,lv}^4\right) \tag{S13}$$

where SW and LW are the incoming shortwave and longwave fluxes (W m⁻²). α_{lv} and ϵ_{lv} are the low vegetation albedo (-) and emissivity (-), respectively, and are grid-average values of the different types of low vegetation in a given grid-cell weighted by the fraction of each type. Table S2 gives the albedo and emissivity of each vegetation type in SVS2.

The sensible heat flux over low vegetation follows the same definition as the SVS1 scheme (Husain et al., 2016):

$$H_{lv} = \frac{\rho_a c_p (T_{s,lv} - T_a)}{R_{a\,lv}} \tag{S14}$$

where ρ_a and T_a correspond to the air density (kg m⁻³) and temperature (K) at the forcing atmospheric level, respectively, c_p is the specific heat of dry air (J kg⁻¹ K⁻¹), and $R_{a,lv}$ is the aerodynamical surface resistance of the low vegetation (s m⁻¹). $R_{a,lv}$ is computed by the surface turbulent scheme of the GEM model (Beljaars and Holtslag, 1991; Delage and Girard, 1992). The latent heat of evaporation from low vegetation follows SVS1 (Husain et al., 2016) and is written as $LE_{lv} = L_V E_{lv}$ where L_v is the latent heat of vaporization (J kg⁻¹), and E_{lv} is the low vegetation vapor flux (kg m⁻² s⁻¹) provided by:

150
$$E_{lv} = \rho_a \frac{h_{lv} q_{sat}(T_{s,lv}) + (1 - h_{lv}) q_a - q_a}{R_{a,lv}} = \rho_a h_{lv} \frac{q_{sat}(T_{s,lv}) - q_a}{R_{a,lv}}$$
(S15)

where ρ_a is the air density (kg m⁻³), h_{lv} is the Halstead coefficient for low vegetation (-) and $q_{sat}(T_{s,lv})$ is the saturated specific humidity (kg kg⁻¹) at temperature $T_{s,lv}$ (K). If the vapor flux is negative (i.e., $q_{sat}(T_{s,lv}) < q_a$), it is assumed that a dew flux occurs at potential rate and h_{lv} is set to 1. When the vapor flux is positive (i.e., $q_{sat}(T_{s,lv}) > q_a$), the Halstead coefficient h_{lv} is calculated as:

155
$$h_{lv} = 1 - \frac{(1 - \delta_{lv})r_s}{R_{a,lv} + r_s}$$
 (S16)

in order to account for both direct evaporation of intercepted water and transpiration from the vegetation. In Eq. S16, r_s is the stomatal resistance, and δ_{lv} is a function of the liquid water intercepted on the low vegetation (e.g., Gouttevin et al., 2015):

$$\delta_{lv} = \left(\frac{W_{r,lv}}{W_{rmax\,lv}}\right)^{2/3} \tag{S17}$$

in which $W_{r,lv}$ is the liquid water content retained by low vegetation (kg m⁻²) and $W_{rmax,lv}$ is a maximum value of $W_{r,lv}$ over which water cannot be retained by vegetation. Water exceedance is transferred to the ground underneath. Following Dickinson (1984), $W_{rmax,lv}$ (kg m⁻²) is proportional to the canopy density: $W_{rmax,lv} = 0.2VAI_{lv}$ where VAI_{lv} is the vegetation area index of low vegetation. A maximal value of 0.25 is imposed to δ_{lv} as in Boone et al. (2017) to represent transpiration in

saturated vegetations. In SVS2, the stomatal resistance, r_s , is computed by the same photosynthesis scheme as in SVS1 (Husain et al., 2016).

The skin conductivity of low vegetation, $\Lambda_{sk,lv}$, provides the thermal connection between the skin level for low vegetation and the upper soil layer (Boussetta et al., 2021). In its current version, SVS2 assumes that $\Lambda_{sk,lv}$ has a constant value of 10 W m⁻² K⁻¹ as in EC-Land (Boussetta et al., 2021). A future version of the model could consider values of $\Lambda_{sk,lv}$ that depend on the atmospheric stability as tested in Trigo et al. (2015).

S1.3 Soil thermal regime and hydrology

170 S1.3.1 Soil layering

180

185

In SVS2, the soil is divided into N_L layers with variable thickness. Both the number of layers and their thickness are configurable. For each soil layer k, three prognostic variables are considered: the soil temperature (T_K, K) , the soil volumetric liquid water content $(w_{l,k}, m^3 m^{-3})$, and liquid water equivalent ice content $(w_{i,k}, m^3 m^{-3})$. In its default configuration, SVS2 uses the same vertical layering as the soil hydrology scheme in SVS1 (Alavi et al., 2016) with a total soil depth of 3 m and 7 layers of increasing thickness $(N_L = 7)$: 0-5 cm, 5-10 cm, 10-20 cm, 20-40 cm, 40-100 cm, 100-200 cm and 200-300 cm.

S1.3.2 Soil thermal properties

The thermal heat capacity and thermal conductivity are parameterized following Peters-Lidard et al. (1998), Boone et al. (2000) and Lawrence and Slater (2008) as functions of the soil moisture and texture with consideration of frozen soils in this formulation. The soil thermal properties are computed for the different soil layers in SVS2. For clarity, the layer indices are not written in the following equations. The layer-averaged soil heat capacity, C, can be written as (J m⁻³ K⁻¹):

$$C = (1 - w_{sat})C_{soil} + w_l c_w \rho_w + w_{ice} c_{ice} \rho_{ice}$$
(S18)

where w_{sat} is saturated volumetric water content (Eq. S26), C_{soil} is the heat capacity of soil matrix (J m⁻³ K⁻¹), c_{ice} and c_w are specific heat capacities of ice and liquid water (J kg⁻¹ K⁻¹). The contribution of air in the soil is neglected due its extremely low volumetric heat capacity compared to other soil components. ρ_w and ρ_{ice} are water and ice densities, respectively. w_l and w_{ice} represent volumetric liquid water and liquid water equivalent ice contents of the soil (m³ m⁻³), respectively. They are related to total volumetric water content through $w = w_l + w_{ice}$. C_{soil} is computed following Peters-Lidard et al. (1998) and Lawrence and Slater (2008):

$$C_{soil} = \begin{cases} \left(\frac{2.128X_{sand} + 2.385 * X_{clay}}{X_{sand} + X_{clay}}\right) * 10^6 & \text{if } X_{sand} + X_{clay} > 0.\\ 733 * 2700. & else \end{cases}$$
(S19)

where X_{sand} and X_{clay} represent the percentage of sand and clay content in soil.

Following Peters-Lidard et al. (1998), soil thermal conductivity, λ , is calculated as a combination of the saturated and dry thermal conductivities weighted by a normalized thermal conductivity K_e (known as the non-dimensional Kersten number):

$$\lambda = K_e \lambda_{sat} + (1 - K_e) \lambda_{dry} \tag{S20}$$

Dry thermal conductivity (W m⁻¹ K⁻¹) is defined as in Johansen (1975):

$$\lambda_{dry} = \frac{0.135\rho_{soil} + 64.7}{2700. - 0.947\rho_{soil}} \tag{S21}$$

where ρ_{soil} represents the bulk density of mineral soil (kg m⁻³): $\rho_{soil} = 2700.(1 - w_{sat})$.

Saturated thermal conductivity (W $m^{-1} K^{-1}$) is written as:

$$\lambda_{sat} = \lambda_{solid}^{1 - w_{sat}} \lambda_{ice}^{w_{sat - \chi_u}} \lambda_w^{\chi_u} \tag{S22}$$

where χ_u represents the unfrozen volume fraction of soil and is defined as:

$$\chi_u = w_{sat} \frac{w_l}{w_l + w_{ice}} \tag{S23}$$

In Eq S22, λ_{ice} represents thermal conductivity of ice, λ_w represents thermal conductivity of water, and thermal conductivity of solid soils is written as

$$\lambda_{solid} = \lambda_q^{1-q} \lambda_o^{1-q} \tag{S24}$$

Following the method of Noilhan et al. (1995) and Peters-Lidard et al. (1998), the non-dimensional quartz content ($0 \le q \le 1$) is expressed as a function of sand content: $q = 0.038 + 0.0095X_{sand}$. The thermal conductivity of quartz, λ_q , is set to 7.7 W m⁻¹ K⁻¹ and thermal conductivity of other minerals, λ_o , varies with q ($\lambda_o = 2.0$ W m⁻¹ K⁻¹ for q > 0.2 and $\lambda_o = 3.0$ W m⁻¹ K⁻¹ for $q \le 0.2$).

Finally, the Kersten number is written as (Boone et al., 2000):

$$K_e = \frac{w_l}{w_l + w_{ice}} (\log(\theta) + 1) + \frac{w_{ice}}{w_l + w_{ice}} \theta$$
(S25)

where θ is the degree of saturation (w/w_{sat}) of the soil layer.

210 S1.3.3 Soil hydraulic properties

SVS2 uses the same soil hydrology module as SVS1 (Alavi et al., 2016). Saturated volumetric water content, w_{sat} , wilting-point volumetric water content, w_{wilt} , and volumetric water content at field capacity, w_{fc} , are calculated based on the percentage of sand and clay contents in soil, X_{sand} and X_{clay} :

$$w_{sat} = 0.489 - 0.00126X_{sand} \tag{S26}$$

$$w_{wilt} = 37.1342 \times 10^{-3} X_{clay}^{0.5} \tag{S27}$$

$$w_{fc} = 89.0467 \times 10^{-3} X_{clay}^{0.3496} \tag{S28}$$

Field capacity for the bottom layer (index N) is determined using an expression developed by Soulis et al. (2011), which takes into account permeable depth (z_b) of the whole overlying soil:

$$w_{fc,N} = \frac{w_{sat,N}}{b-1} \left(\frac{\Psi_{sat,N}b}{z_b}\right) \left[(3b+2)^{(b-1/b)} - (2b+2)^{(b-1)/b} \right]$$
(S29)

where Ψ_{sat} is saturated soil water potential and b is the slope of the water retention curve calculated based on Brooks and Corey (1966):

$$\Psi_{sat} = 0.01 \times 10^{-0.0131X_{sand} + 1.88} \tag{S30}$$

225

$$b = 0.137X_{clay} + 3.501 (S31)$$

Saturated hydraulic conductivity, K_{sat} , is also derived from Brooks and Corey (1966):

$$K_{sat} = 7.0556 \times 10^{-6} \times 10^{0.0153X_{sand} - 0.884}$$
(S32)

In the presence of ice, K_{sat} and w_{sat} are modified as described in Sect. S1.3.7.

230 S1.3.4 Impact of soil organic matter

Soil organic matter is not considered by default in SVS2. An optional parametrization can be activated to simulate its impact on the hydraulic and thermal properties of the soil. The GSDE database (Shangguan et al., 2014) is used to obtain the fraction of organic content of each soil layer (f_{soc}). This fraction is derived from soil organic carbon content (OC, % of weight), bulk soil density (ρ_{bulk} , kg m⁻³), and gravel volumetric content (GRAV, % of volume):

235
$$f_{soc} = \rho_{bulk} \frac{OC}{100} (1 - \frac{GRAV}{100}) / \rho_{so,max}$$
 (S33)

where $\rho_{so,max}$ is the maximum soil carbon density taken equal to 130 kg m⁻³ as in Lawrence and Slater (2008). The fraction of organic content of each soil layer is used to determine the average soil layer properties between the mineral properties and organic properties using either weighted arithmetic or geometric averages following Decharme et al. (2016). A future version of SVS2 will used information on soil organic matter from the SoilGrids 2.0 database (Poggio et al., 2021).

Thermal and hydraulic properties of the organic soil column are calculated following Decharme et al. (2016), i.e. the organic part of soil follows an idealized soil profile, with organic soil properties in the first 10 cm being 100 % fibric soil, the organic soil properties below the depth of 1 m being 100 % sapric soil, and organic soil properties in between transition from the two soil types with an exponential decay:

$$\alpha_{soc} = \alpha_{fibric} \left(\frac{z(i)}{d_{sapric}} \right)^{\beta} \quad \text{with } \beta = \frac{\ln(\alpha_{sapric}/\alpha_{fibric})}{\ln(d_{sapric}/d_{fibric})}$$
 (S34)

where α_{soc} , α_{sapric} , and α_{fibric} represent the hydraulic and thermal properties of the soil accounting for the organic carbon content, for 100% sapric soil and 100% fabric soil, respectively. d_{sapric} and d_{fibric} are the depth of the fibric and sapric of the organic soil profiles, taken equal to 1 m and 0.01 m, respectively, following Decharme et al. (2016). The reader is referred to Table 1 of Decharme et al. (2016) for the values of the hydraulic and thermal properties of fibric and sapric soils.

S1.3.5 Soil heat diffusion

260

265

250 The governing equation for heat from the surface down through the soil column is expressed as in Boone et al. (2000) and Decharme et al. (2011):

$$C\frac{\partial T_{soil}}{\partial t} = \frac{\partial G}{\partial z} + \Phi \tag{S35}$$

where C is soil heat capacity (Eq. S18, J m⁻³ K⁻¹), T_{soil} is soil temperature (K), G is soil heat flux (W m⁻²), Φ is a latent heat source/sink resulting from phase transformation of soil water (J m⁻³ s⁻¹), and soil depth, z (m), is increasing downward. Heat flow is along the thermal gradient, so that G can be expressed as:

$$G = \lambda \frac{\partial T_{soil}}{\partial z} \tag{S36}$$

where λ is soil thermal conductivity (Eq. S20).

The total heat flux from the surface tiles towards the upper soil temperature, G_0 is computed as a weighted average of heat fluxes from 5 land surface tiles that are thermally coupled with the underlying soil (Table S1) as in Boussetta et al. (2021):

$$G_{0} = f_{g,sno}G_{sno} + f_{g,snhv}G_{snhv} + f_{g,lv}\Lambda_{sk,lv}\left(T_{s,lv} - T_{soil,1}\right) + f_{g,bg}\Lambda_{sk,bg}\left(T_{s,bg} - T_{soil,1}\right) + f_{g,ghv}\Lambda_{sk,ghv}\left(T_{s,ghv} - T_{soil,1}\right)$$

$$\tag{S37}$$

where G_{sno} and G_{snhv} are heat fluxes (W m⁻²) at the bottom of the snowpack in open terrain and below high vegetation respectively, $\Lambda_{sk,lv}$, $\Lambda_{sk,bg}$, $\Lambda_{sk,ghv}$ are the skin thermal conductivities for low vegetation, exposed bare ground, and bare ground below high vegetation (W m⁻¹ K⁻¹), respectively, and $T_{s,lv}$, $T_{s,bg}$ and $T_{s,ghv}$ are skin temperatures for low vegetation, exposed bare ground and bare ground below high vegetation (K), respectively. $f_{g,*}$ represents the fraction of the respective land surface tiles seen from the underlying ground as defined in Table S1.

SVS2 considers two options to compute the heat flux at the bottom of the soil column G_N (W m⁻²). The first option considers a zero-flux lower boundary condition ($G_N = 0$ W m⁻²) which is suitable if the soil column is sufficiently deep (e.g., Decharme et al., 2013). The second option uses a fixed temperature forcing at the bottom of the soil column representative of the mean annual temperature. This option requires less soil layers than the zero-flux approach and reduces computational expense and memory/storage requirements. This is the default option in SVS2. When SVS2 distributed simulations are carried out across North America, the model uses a climatology of deep soil temperature derived from the Canadian Regional Climate Model version 5 (Martynov et al., 2013).

The numerical solution for Eq. S35 uses a fully-implicit finite-difference scheme applied to an unstaggered vertical grid as described in Sect. S1.3.1. For details of the discretization and boundary conditions, the reader should refer to Sect. S2.2. Tem-

275 perature is computed at the middle of each layer and considered uniform within the layer, while the heat fluxes are calculated at the layers' interfaces.

S1.3.6 Soil hydrology

The evolutions of volumetric soil liquid and ice water contents (w_l and w_i , respectively) in different soil layers are calculated using the following equations:

$$280 \quad \frac{\partial w_l}{\partial t} = \frac{\partial F}{\partial z} - \frac{\Phi}{L_f \rho_w} - \frac{S_l}{\rho_w} \tag{S38}$$

$$\frac{\partial w_i}{\partial t} = \frac{\Phi}{L_f \rho_w} \tag{S39}$$

in which F is the liquid water flow between soil layers (m s⁻¹), Φ is latent heat source/sink resulting from soil freezing and thawing (J m⁻³ s⁻¹) and S_l is a sink term (kg m⁻³ s⁻¹) resulting from lateral flow, bare-ground evaporation and transpiration from vegetation. F(z) is calculated as in SVS1 (Alavi et al., 2016) using Darcy's equation for one-dimensional fluid flow:

285
$$F(z) = K(z) \left(\frac{d\Psi}{dz} + 1\right)$$
 (S40)

where K(z) represents hydraulic conductivity (m s⁻¹) and Ψ the soil water potential at depth z (m):

$$K(z) = K_{sat} \left[\frac{w_l}{w_{sat}} \right]^{2b+3} \tag{S41}$$

$$\Psi(z) = \Psi_{sat} \left[\frac{w_l}{w_{sat}} \right]^{-b} \tag{S42}$$

where K_{sat} and Ψ_{sat} represent saturated hydraulic conductivity (m s⁻¹) (Eqs. S32) and saturated soil water potential (m) (Eq. S30), respectively. b is defined following Brooks and Corey (1966) and is given in Eq. S31.

The water flux reaching the ground surface is obtained by weighting contributions of each land surface tile and can be written as:

$$W_{in,surf} = f_{g,sno}R_{sno} + f_{g,snhv}R_{snhv} + f_{g,bg}PR + f_{g,ghv}PR_c + f_{g,lv}R_{lv}$$
(S43)

where R_{sno} is the rate of liquid water runoff at the bottom of the snowpack above bare ground and low vegetation (m s⁻¹), R_{snhv} the rate of liquid water runoff at the bottom of the snowpack below high vegetation (m s⁻¹), PR is the rate of liquid precipitation falling in open terrain (m s⁻¹), PR_c is the rate of throughfall and dripping below the high vegetation (m s⁻¹), R_{lv}

is the liquid dripping rate of water intercepted on snow-free low vegetation (m s⁻¹) (Sect. S1.2.3). $f_{g,*}$ represents the fraction of respective land surface tiles seen from the underlying ground as defined in Table S1.

The flux of liquid water infiltrating into the soil (m s $^{-1}$) is then given by:

$$F_0 = W_{in.surf} - RU_{surf} \tag{S44}$$

where RU_{surf} is the surface runoff (m s⁻¹). It is calculated as in Alavi et al. (2016) based on the fraction of the surface that is saturated and is generated when either soil moisture exceeds saturation or when precipitation rate exceeds K_{sat} of the first soil layer. At the bottom of the soil column the amount of liquid water leaving the lowest layer, F_N (m s⁻¹), corresponds to the baseflow, calculated when soil water content exceeds the water content at field capacity for the bottom layer (Eq. S29) (Alavi et al., 2016).

The term S_l (kg m⁻³ s⁻¹) in Eq. S38 represents the loss of soil water content associated with lateral flow, evaporation from exposed bare ground (E_{bg} , kg m⁻² s⁻¹) and bare ground below high vegetation (E_{ghv} , kg m⁻² s⁻¹), and transpiration from high and low vegetation ($E_{tr,hv}$ and $E_{tr,lv}$, respectively, kg m⁻² s⁻¹). Evaporation from exposed bare ground and bare ground below high vegetation only affects the evolution of soil moisture of the upper soil layer as in SVS1 (Alavi et al., 2016). S_l for the different soil layers can be expressed as:

$$S_{l,i} = \begin{cases} (1/\Delta z_i) \times [f_{a,bg} E_{bg} + f_{a,ghv} E_{ghv} + f_{root,1} (f_{a,lv} E_{tr,lv} + f_{a,hv} E_{tr,hv}) + Lat_1] & \text{if } i = 1\\ (1/\Delta z_i) \times [f_{root,i} (f_{a,lv} E_{tr,lv} + f_{a,hv} E_{tr,hv}) + Lat_i] & \text{if } i = 2, \dots, N \end{cases}$$
(S45)

where f_{root} is the fraction of roots in each soil layer based on a pre-defined root-zone profile (Schenk and Jackson, 2005), $f_{a,*}$ represents the fraction of the respective land surface tiles seen from the underlying ground as defined in Table S1, and Δz_i is the thickness of layer i (m). As in SVS1 (Alavi et al., 2016), lateral flow, Lat (kg m⁻² s⁻¹), is based on the parameterization of subgrid-scale interflow described in Soulis et al. (2011) for a tilted landscape.

S1.3.7 Soil freezing and thawing

305

310

SVS2 uses the approach of Boone et al. (2000) and Decharme et al. (2016) to simulate the evolution of soil ice content and its impact on soil temperature. A sequential approach is used: (i) soil temperature is first computed using Eq.S35, (ii) phase change term Φ in Eqs. S35, S38 and S39 are then computed, and (iii) soil temperature, liquid water and ice content are finally adjusted accordingly. During phase change, the total water content in each soil layer, $w = w_i + w_l$, is conserved.

SVS2 takes into account the depression of the freezing point. Soil water matrix potential $\Psi(T)$ (m) for each soil layer can be written as in Fuchs et al. (1978) and Niu and Yang (2006):

$$\Psi(T) = \frac{L_f(T_{soil} - T_f)}{gT_{soil}} \tag{S46}$$

where T_{soil} and T_f are soil temperature and freezing point (K), respectively; L_f is latent heat of fusion (J kg⁻¹) and g is gravitational acceleration (m s⁻²). Using the analogy between freezing–thawing processes and drying–wetting processes with

regard to the dependence of soil matric potential on liquid water content (Eq. S30) (e.g., Kurylyk and Watanabe, 2013), the expression for the freezing-point depression equation is:

$$w_{l,max} = w_{sat} \left[\frac{L_f(T_{soil} - T_f)}{gT_{soil} \Psi_{sat}} \right]^{-1/b}$$
(S47)

where $w_{l,max}$ is the maximum liquid water content when soil temperature is below freezing. For a given liquid water content and an associated soil liquid water potential, Ψ , the maximum temperature at which ice exists in the soil, can be derived as:

$$T_{max} = \frac{L_f T_f}{L_f - g\Psi} \tag{S48}$$

The latent heat source/sink resulting from soil freezing and thawing, Φ , in Eqs. S35, S38 and S39 is then derived as in Boone et al. (2000): $\Phi = \Phi_f - \Phi_m$ where Φ_f is the contribution from soil freezing and Φ_m the contribution from soil thawing:

335
$$\Phi_f = \min\left[\max(0, T_{max} - T_{soil})c_{ice}\rho_{ice}, L_f\rho_w\max(0, w_l - w_{l,max})\right]/\tau_i$$
 (S49)

$$\Phi_m = \min\left[\max(0, T_j - T_{max})c_{ice}\rho_{ice}, L_f\rho_w w_i\right]/\tau_i \tag{S50}$$

where c_{ice} and ρ_{ice} are specific heat capacity (J kg⁻¹ K⁻¹) and density (kg m⁻³) of ice, respectively. τ_i is a time parameter (s) that represents the characteristic time scale for phase changes (Giard and Bazile, 2000). It is set to 3300 s as in Boone et al. 340 (2000). The surface insulation coefficient from Giard and Bazile (2000) in the formulation of Φ_f and Φ_m is not used in the current version of SVS2.

Temperature and soil water profiles are updated at the end of the time step, Δt (s), using the calculated phase change term, Φ , as in Boone et al. (2000):

$$T_{soil}^{n+1} = T_{soil}^{n'} + \frac{\Delta t \Phi}{c_h} \tag{S51}$$

345

$$w_l^{n+1} = w_l^{n'} - \frac{\Delta t \Phi}{L_f \rho_w} \tag{S52}$$

$$w_i^{n+1} = w_i^{n'} + \frac{\Delta t \Phi}{L_f \rho_w} \tag{S53}$$

where values at n + 1 represent values at the end of the time step whereas values at n' represent intermediate values obtained after solving Eqs. S35 and S38.

The presence of frozen soil in SVS2 ($w_i > 0$) modifies the hydraulic conductivity at saturation and the soil porosity. The saturated hydraulic conductivity in the presence of frozen soil is written as $K_{satc} = f_{ice}K_{sat}$. f_{ice} is a parameter that aims at

reducing K_{sat} in presence of frozen water in the soil (e.g., Kurylyk and Watanabe, 2013). It is computed as in the CLASS land surface scheme (Ganji et al., 2017):

355
$$f_{ice} = \left[1 - \min\left(1., \frac{w_i}{w_{sat}}\right)\right]^2 \tag{S54}$$

Volumetric liquid water content at saturation is also reduced assuming that frozen water becomes part of the soil matrix (Zhao et al., 1997):

$$w_{satc} = w_{sat} - w_i ag{S55}$$

Evapotranspiration is also indirectly impacted due to the change in liquid water content when freezing or thawing occurs.

360 S1.4 Sublimation of intercepted snow (O2F) option

In SVS2, the "open to forest" option (O2F) is activated when the model is driven by meteorological forcing transferred from adjacent open terrain (Sect. 2.3.6 of the main manuscript). With this option, the energy balance of the canopy is not calculated, the model estimates the sublimation of intercepted snow following Pomeroy et al. (1998) and Essery et al. (2003). In this approach, the sublimation rate coefficient of an ice particle, V_s (s^{-1}), accounting for shortwave radiative heat is first calculated as

$$V_s = \frac{\frac{2\pi r}{m} \left(\frac{\rho_a}{\rho_s} - 1\right) - S^* J}{h_s J + \frac{1}{D\rho_s S_h}} \tag{S56}$$

with r the radius of an ideal ice sphere taken equal to 0.5 mm, ρ_a and ρ_s are densities of air and saturated water vapour density (kg m $^{-3}$), respectively, m is the mass of the ice sphere (kg), D is diffusivity of water vapor in air ($D=2.06 \mathrm{x} 10^{-5} \left(\frac{T_a}{273.15}\right)^{1.75}$, m 2 s $^{-1}$), and S_h is the Sherwood number ($S_h=1.79+0.606\left(\frac{2ru}{\mu}\right)^{0.5}$ with u the wind speed within the canopy, m s $^{-1}$, and μ the air viscosity, m 2 s $^{-1}$).

 V_s is then scaled up to the total sublimation rate of the snow on the canopy per unit ground of the high vegetation tile:

$$E_{rs} = C_e \frac{S_{nv}}{m} V_s \tag{S57}$$

with C_e a scaling coefficient empirically determined by Pomeroy and Schmidt (1993) ($C_e = 0.0114 \left(\frac{S_{nv}}{S_{max}^{max}}\right)^{-0.37}$).

S2 Model numerical implementation

375 **S2.1 Overview**

365

Figure S2 presents a comprehensive overview of the sequential computational framework and order of operations that occur within a single model time step of SVS2. It is important to note that this computational structure and sequence of operations

remain consistent with those originally established in SVS (Alavi et al., 2016; Husain et al., 2016), ensuring continuity and compatibility with previous modeling efforts.

SVS2 employs a sequential computational approach to calculate the energy and mass balance equations across the integrated soil-vegetation-snow column. To ensure numerical stability, the model utilizes implicit numerical schemes for (i) computing the energy balance of high vegetation, (ii) solving heat diffusion processes within the snowpack, (iii) determining heat diffusion through the soil column and (iv) modeling soil hydrology. Section S2.2 provides a description of the numerical techniques employed in SVS2 for solving heat diffusion in the soil column, while Section S2.3 presents the numerical implementation for computing the energy balance of high vegetation. The heat diffusion processes occurring within the stratified snowpack are solved using the implicit time integration scheme implemented in Crocus (Boone and Etchevers, 2001; Vionnet et al., 2012). Finally, the temporal evolution of soil moisture content throughout the various soil layers is computed numerically using the same fourth-order Runge-Kutta finite difference method that was implemented in SVS (Alavi et al., 2016). At the conclusion of each time step, after the new vertical soil temperature and liquid water content profiles have been determined, the model evaluates potential phase changes (freezing or thawing) that may have occurred in the soil. Following this evaluation, the temperature profile and soil liquid water and ice contents are updated accordingly, following the methodology described in Boone et al. (2000).

S2.2 Heat diffusion equation in the soil

380

385

390

395

In SVS2, the soil column is divided into N_L predefined layers in SVS2. For each soil layer, soil temperature evolves due to vertical heat transport and phase changes, with surface conditions determined by energy budget closure. The heat diffusion equation (Eq. S35) is solved using a fully-implicit finite-difference scheme on an unstaggered vertical grid. Temperature is defined at the middle of each layer and assumed uniform within the layer; each layer is assumed to have a constant conductivity and heat capacity. The numerical scheme can accommodate arbitrary layer spacing. The finite-difference representation of Eq. S35 is:

$$400 \quad C_k \frac{T_k^+ - T_k}{\Delta t} = \frac{1}{\Delta z_k} \left\{ \overline{\lambda}_k \left[(1 - \beta) \frac{T_{k+1} - T_k}{\delta z_k} + \beta \frac{T_{k+1}^+ - T_k^+}{\delta z_k} \right] - \overline{\lambda}_{k-1} \left[(1 - \beta) \frac{T_k - T_{k-1}}{\delta z_{k-1}} + \beta \frac{T_k^+ - T_{k-1}^+}{\delta z_{k-1}} \right] \right\} + \Phi_k \quad (S58)$$

Subscripts index the spatial grid (up to N_L layers), superscripts + represent the value at the end of the time step, Δt is the time step (s), Δz is layer thickness (m), δz is the distance between mid-points of contiguous layers, and β is a parameter which determines the "implicitness" of the time-stepping scheme ($\beta = 0$ means an explicit, forward-in-time, centered-in-space scheme, $\beta = 0.5$ yields the Crank-Nicholson scheme, and $\beta = 1$ yields the fully-implicit scheme which is unconditionally stable). In SVS2, β is set to 1 to allow long time steps and small layer spacing. The rest of the numerical discretization is presented assuming that $\beta = 1$. Φ_k is an internal heat sink/source resulting from phase transformation of soil water and is neglected for the first evaluation of a temperature profile. Once the new temperature profile has been determined, phase change is evaluated and the profile is updated based on Boone et al. (2000) as detailed in Sect. S1.3.7.

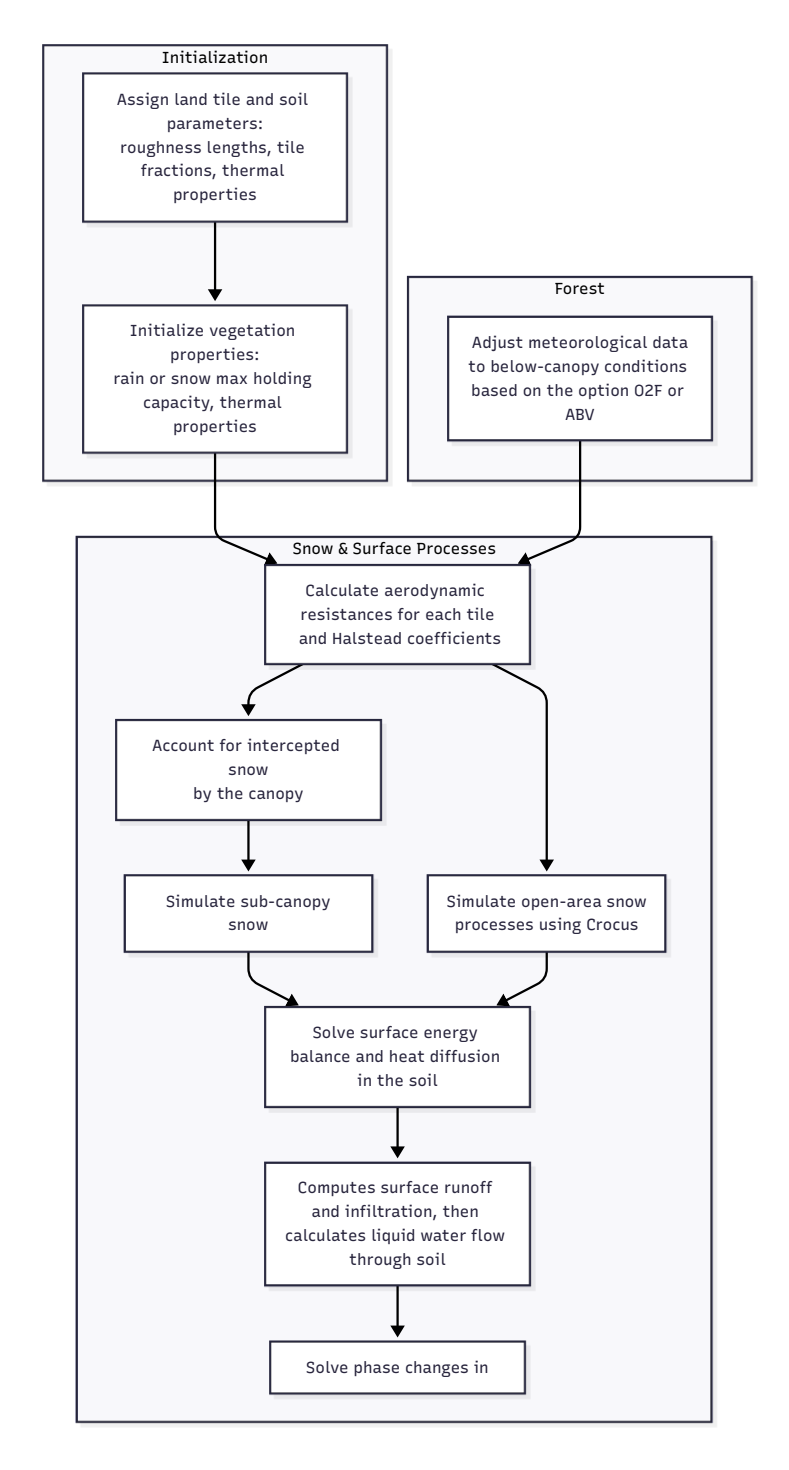


Figure S2. Flowchart showing the order of operations within one model time step of SVS2

 $\overline{\lambda}_k$ is the interfacial thermal conductivity expressed as:

410
$$\overline{\lambda}_{k} = \begin{cases} \lambda_{k} \frac{\Delta z_{k}}{\Delta z_{k} + \Delta z_{k+1}} + \lambda_{k+1} \frac{\Delta z_{k+1}}{\Delta z_{k} + \Delta z_{k+1}} & \text{if } k < N_{L} \\ \lambda_{N_{L}} & \text{if } k = N_{L} \end{cases}$$
(S59)

The distance between mid-points of contiguous layer is computed as:

$$\delta z_k = \begin{cases} \frac{\Delta z_k + \Delta z_{k+1}}{2} & \text{if } k < N_L \\ \Delta z_{N_L} & \text{if } k = N_L \end{cases}$$
 (S60)

Without the phase change term Φ_k and considering β =1, Equation S58 can be rewritten as:

$$T_k^+ + \frac{\Delta t \overline{\lambda}_k}{C_k \Delta z_k \delta z_k} T_k^+ + \frac{\Delta t \overline{\lambda}_{k-1}}{C_k \Delta z_k \delta z_{k-1}} T_k^+ - \frac{\Delta t \overline{\lambda}_k}{C_k \Delta z_k \delta z_k} T_{k+1}^+ - \frac{\Delta t \overline{\lambda}_{k-1}}{C_k \Delta z_k \delta z_{k-1}} T_{k-1}^+ = T_k$$
 (S61)

This equation can be rewritten is the form:

$$a_k T_{k-1}^+ + b_k T_k^+ + c_k T_{k+1}^+ = d_k (S62)$$

where

$$a_k = -\frac{\Delta t \overline{\lambda}_{k-1}}{C_k \Delta z_k \delta z_{k-1}}; \quad b_k = 1 - a_k - c_k; \quad c_k = -\frac{\Delta t \overline{\lambda}_k}{C_k \Delta z_k \delta z_k}; \quad d_k = T_k$$
(S63)

Equation S62 can be written as a N_L row tri-diagonal matrix and solved numerically.

420 S2.3 Energy balance of high vegetation

An implicit scheme is used to solve for canopy temperature (Eq. 2 in the main manuscript):

$$C_v \frac{T_v^+ - T_v}{\Delta t} = SW_{net}^+ + LW_{net}^+ + H_v^+ + LE_v^+ + L_f \Phi_v^+$$
(S64)

where variables with the superscripts + are at the end of the time step Δt . A first-order Taylor expansion was used to linearize some terms at then end of Δt :

425
$$T_v^{+4} = T_v^4 + 4T_v^3(T_v^+ - T_v)$$
 (S65a)

$$q_{sat}(T_v^+) = q_{sat}(T_v) + \frac{dq_{sat}}{dT}|_{T=T_v}(T_v^+ - T_v)$$
(S65b)

Hence, the terms in Eq. S64 after linearization become:

$$LW_{net}^{+} = \sigma_f (LW_{in} + \sigma T_s^4) - 8\sigma_f \sigma T_v^3 T^{+} + 6\sigma\sigma_f T_v^4$$
(S66a)

$$LE_v^+ = \frac{\rho L}{R_{av}} (q_a - q_{sat}(T_v)) - \frac{dq_{sat}}{dT} |_{T = T_v} (T_v^+ - T_v)$$
(S66b)

with $L = h_v(1 - p_{nv})L_v + p_{nv}L_s$ from Eq.8 of the main manuscript.

$$H_v^+ = \frac{\rho L}{R_{av}} (T_a - T_v^+) \tag{S66c}$$

Finally, the linearized energy balance equation becomes:

435
$$AT_v^+ = BT_v + C$$
 (S67)

where A, B, and C are matrices expressed as:

$$A = \frac{C_v}{\Delta t} + 8\sigma_f \sigma T_v^3 + \frac{\rho C_p}{R_{av}} + \frac{\rho L}{R_{av}} + \frac{dq_{sat}}{dT}|_{T=T_c}$$
(S68a)

$$B = 6\sigma\sigma_f T_v^3 + \frac{\rho L}{R_{av}} \frac{dq_{sat}}{dT}|_{T=T_c} + \frac{C_v}{\Delta t}$$
 (S68b)

440

$$C = SW_{net}^{+} + \Phi_{v}^{+} + \sigma_{f}LW_{in} + \sigma_{f}\sigma T_{s}^{4} + \frac{\rho C_{p}}{R_{av}}T_{a} + \frac{\rho L}{R_{av}}(q_{a} - q_{sat}(T_{v}))$$
 (S68c)

and SW_{net}^+ and Φ_v^+ stay the same as Eq. 4 and Eq. 15 in the main manuscript using the values at the end of the time step, respectively.

S2.4 Surface energy balance of exposed bare ground, bare ground below high vegetation and low vegetation

Equations of surface energy balance for exposed bare ground (Eq. S3), bare ground below high vegetation (Eq. S11) and low vegetation (Eq. S12) are similar and can be written in the general form:

$$R_n - H - LE = \Lambda_{sk} \left(T_s - T_{soil.1} \right) \tag{S69}$$

Using a first-order Taylor expansion for surface temperature as in Eq. S65a, net radiation fluxes can be written as:

$$R_n = (1 - \alpha)SW + \epsilon \left(LW - 4\sigma T_s^3 T_s^+ + 3\sigma T_s^4\right) \tag{S70}$$

where α is surface albedo, ϵ is surface emissivity, σ is the Stefan Boltzmann constant, and SW and LW are incoming shortwave and longwave radiations respectively. Superscript + represents the value at the end of the time step.

Using Eq. S65b, the latent heat flux for exposed bare ground and bare ground below high vegetation can be written as:

$$LE = \frac{\rho_a L_{eff}}{R_a} \left[HR \left(q_{sat} \left(T_s \right) + \frac{dq_{sat}}{dT} \times \left(T_s^+ - T_s \right) \right) - q_a \right]$$
(S71)

where HR is the relative humidity of the corresponding bare ground surface (see Eq. S10 for exposed bare ground).

For snow-free low vegetation, the latent heat flux can be written as:

$$LE = \frac{\rho_a L_{eff} h_{lv}}{R_a} \left[q_{sat}(T_s) + \frac{dq_{sat}}{dT} \times (T_s^+ - T_s) - q_a \right]$$
(S72)

where h_{lv} is the Halstead coefficient for low vegetation (Eq. S16).

The sensible heat flux can be written as a function of T_s^+ :

$$H = \frac{\rho_a c_p (T_s^+ - T_a)}{R_a} \tag{S73}$$

460 Finally, Eq. S69 can be reorganized and T_s^+ can be written as:

$$T_s^+ = \frac{A(T_s)}{B(T_s)} \tag{S74}$$

For exposed bare ground and bare ground below high vegetation, $A(T_s)$ and $B(T_s)$ can be written as:

$$A(T_s) = \Lambda_{sk} T_{soil,1} + (1 - \alpha)SW + \epsilon LW + 3\epsilon\sigma T_s^4 + \frac{\rho_a c_p}{R_a} T_a + \frac{\rho_a L_{eff}}{R_a} \left[q_a - HR\left(\frac{dq_{sat}}{dT} T_s - q_{sat}\right) \right]$$
 (S75)

$$465 \quad B(T_s) = \Lambda_{sk} + 4\epsilon\sigma T_s^3 + \frac{\rho_a C_p}{R_a} + \frac{\rho_a L_{eff} HR}{R_a} \frac{dq_{sat}}{dT}$$
(S76)

For snow-free low vegetation, $A(T_s)$ and $B(T_s)$ can be written as:

$$A(T_s) = \Lambda_{sk} T_{soil,1} + (1 - \alpha)SW + \epsilon LW + 3\epsilon\sigma T_s^4 + \frac{\rho_a c_p}{R_a} T_a + \frac{\rho_a L_{eff} h_{lv}}{R_a} \left[q_a - q_{sat} + \frac{dq_{sat}}{dT} T_s \right]$$
(S77)

$$B(T_s) = \Lambda_{sk} + 4\epsilon\sigma T_s^3 + \frac{\rho_a c_p}{R_a} + \frac{\rho_a L_{eff} h_{lv}}{R_a} \frac{dq_{sat}}{dT}$$
(S78)

470 S3 Additional point scale simulations

S3.1 Evaluation at Marmot Creek research basin

S3.1.1 Methods

SVS2 was evaluated at two sites at Marmot Creek Research Basin, Kananaskis Country (Alberta, Canada). The two sites, Upper Clearing (UC) and Upper Forest (UF), are about 200 m away from each other. UC (50°57'N, 115°09'W; 1860 m above

sea level) is in a clearing of approximately 56 m in diameter. UF is in the forest adjacent to the clearing. The reader is referred to Musselman et al. (2015) for further site details. Meteorological forcing used to drive the model were published in Fang et al. (2019). Precipitation phase was determined using the parametric equation of Harder and Pomeroy (2013) that has been developed at Marmot Creek.

Two experiments were conducted between September 2012 and June 2016. The first experiment one used meteorological forcing at the tripod station at UC \sim 2 m above the ground surface; these forcing were used to simulate sub-canopy snow using the O2F option (Sect. 2.3.6 of the main manuscript). The second experiment used the meteorological observations for the tower at UC (denoted UCT) at \sim 20 m above the ground surface; sub-canopy snow at UF was simulated from UCT using the ABV option (Sect. 2.3.6 of the main manuscript). Meteorological observations were also collected at UF below the canopy at \sim 2 m above the ground and are used to evaluate simulated meteorological variables below the canopy with the two canopy options (O2F ans ABV). Snow simulations in the clearing and sub-canopy were evaluated against in-situ snow survey data of snow depth and SWE (Fang et al., 2019).

SVS2/Crocus relied on the default configuration of the model (Lafaysse et al., 2017), as per evaluation at Snow Crested Butte (see Sect. 4.1 of the main manuscript). The updated snow albedo parameterization of Gaillard et al. (2025) and changes of Woolley et al. (2024) specific to arctic environments were not activated since no impact was expected in this environment. In the clearing (UC), vegetation was considered to be composed of short grass with a height of 20 cm and evergreen needle-leaf trees are considered in the forest (UF) with an average tree height of 13 m and a canopy density of approximately 80 %. The canopy density was estimated using the Global Tree Canopy Cover database (Hansen et al., 2013). The percentage of clay and sand in each of the seven soil layers were taken from the Global Soil Dataset for use in Earth System Models (Shangguan et al., 2014). The initial temperature and initial water content of soil layers were taken from measurements. Finally, the initial temperature of the canopy, T_c , was chosen to be equal to the air temperature.

S3.1.2 Results and discussions

480

485

490

495

500

505

Figure S3 presents the simulated snow depth and snow water equivalent (SWE) at the two sites between 2012 and 2016, using two configurations of the SVS2 canopy module (O2F and ABV). Simulations slightly differ in the open due to differences in meteorological forcings between the tower and tripod at the surface. For the four winters, the model in both configurations well captured reduced snow accumulation below the forest due to snow interception and sublimation of intercepted snow. The ABV option usually simulated larger snow depths and SWE during the accumulation period than the 02F option. This is explained by differences in the simulated sublimation rates of snow intercepted in the canopy (Fig. S4). Using the ABV option, less sublimation of intercepted canopy snow is estimated by the model, resulting in more unloading of intercepted snow and thus, more snow on the ground. In the ABV option, sublimation rates of intercepted snow are computed from the latent heat flux between the vegetation and the atmospheric forcing level as in Koivusalo and Kokkonen (2002) and Gouttevin et al. (2015), whereas in the O2F option it is computed using the approach of Pomeroy et al. (1998) (Sect. S1.4). Improved SWE estimation at UF with the O2F option suggests that the sublimation rate at this site is better represented using the approach

of Pomeroy et al. (1998). Further investigations are required with SVS2 to reduce the uncertainties associated with sublimation of intercepted snow.

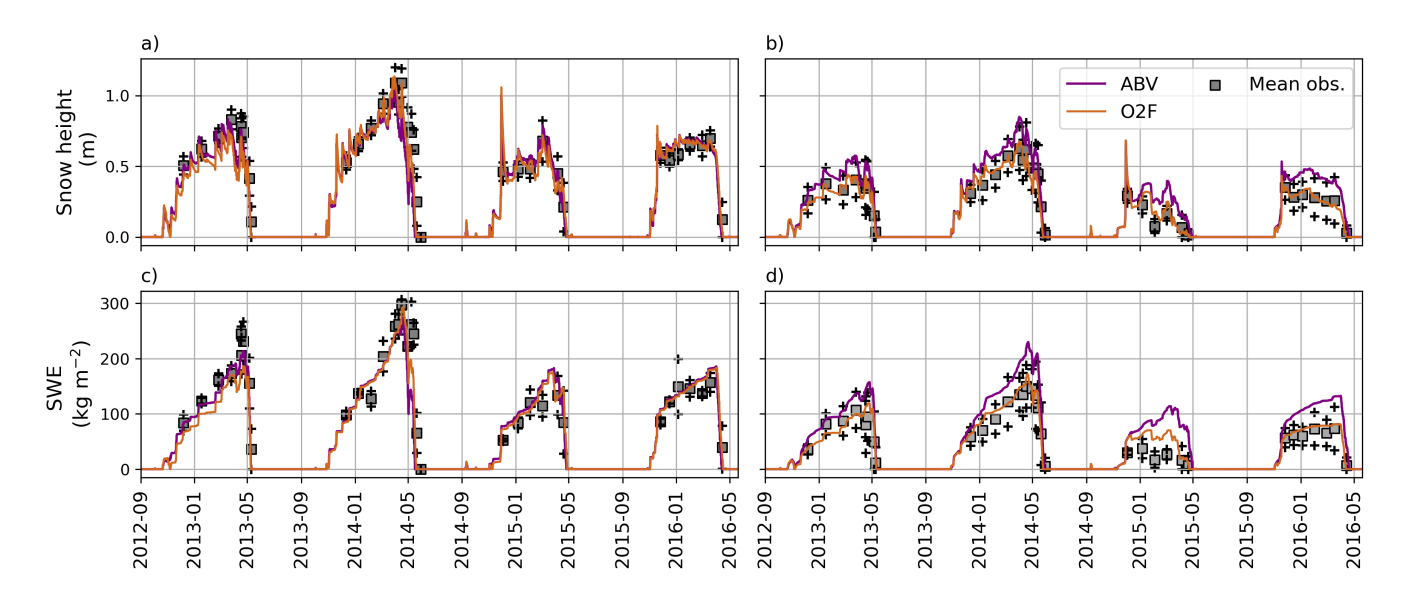


Figure S3. Simulated snow depth and SWE between September 2012 and June 2016 at (a,c) the open site, Upper Clearing (UC), and (b,d) the forest site, Upper Forest (UF). The O2F simulations use meteorological forcing from the tripod at ~ 2 m above the ground at Upper Clearing and the ABV simulations use meteorological observations at ~ 20 m above the ground at Upper Clearing. The squares represent the average of the snow depth or SWE of the snow surveys and the crosses represent the mean of the observations \pm one standard deviation.

Table S3 summarizes the biases and RMSE computed between simulated wind speed, shortwave radiation, and longwave radiation and observations below the canopy and between observations in the open and those below the canopy. This comparison aims at quantifying the impact of the canopy module (in configuration O2F and ABV) on the atmospheric forcing provided to the land surface tiles below high vegetation (bare ground and snowpack below high vegetation). Results show a clear improvement (reduction in absolute bias and RMSE) when these modules are activated compared to using observed forcing collected in open terrain to simulate snow under the canopy. Both configurations enhance (decrease) longwave (shortwave) radiation below high vegetation compared to those of the adjacent open terrain. Similar performances are obtained with the O2F and ABV configurations.

S3.2 Evaluation of snow interception in trees at Umpqua National Forest (Oregon, USA)

Storck et al. (2002) measured intercepted snow on two Douglas Fir trees in the Umpqua National Forest, Oregon, USA. Meteorological forcing at this maritime site and were collected in an adjacent open terrain between 1997 and 1998. The O2F option was used in SVS2/Crocus to simulate the snowpack under the canopy. The reader is referred to Lundquist et al. (2021) and Storck et al. (2002) for a further description of the meteorological forcing. The phase partitioning method of Wang et al. (2019) was used to divide total precipitation into solid and liquid precipitation. Figure S5 shows a comparison

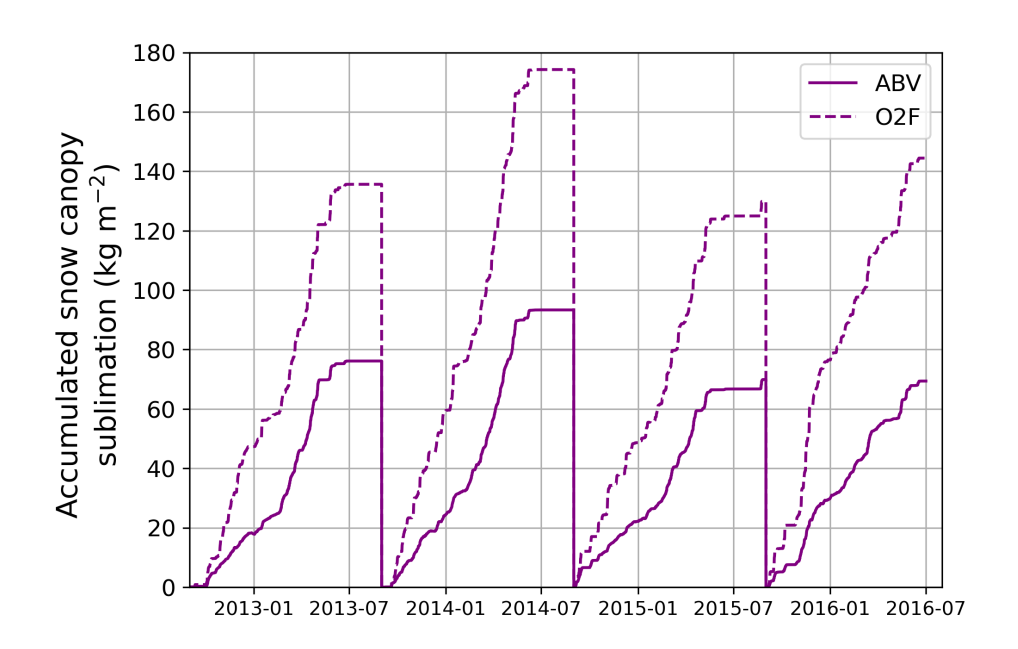


Figure S4. Accumulated sublimation of intercepted snow for four consecutive winters simulated at Upper Forest (UF) using two configurations of the SVS2 canopy module (02F and ABV). The sublimation amounts are reset to zero on October 1^{st} of each year.

Table S3. Bias and RMSE of incoming shortwave radiation (SW), incoming longwave radiation (LW), and wind speed below the canopy between the simulations with the two options ABV and O2F as well as between the observations in the open and those below the canopy.

| | Source | Bias | RMSE |
|---------------------|--------|-------|-------|
| SW | ABV | 1.1 | 34.6 |
| (W m^{-2}) | O2F | 0.1 | 34.1 |
| (WIII) | UCT | 122.8 | 241.7 |
| | UC | 123.3 | 246.0 |
| LW | ABV | 3.7 | 8.9 |
| (W m^{-2}) | O2F | 3.7 | 7.4 |
| (W III) | UCT | -47.1 | 63.3 |
| | UC | -47.1 | 63.5 |
| Wind speed | O2F | -0.01 | 0.2 |
| $(m s^{-1})$ | UC | 1.0 | 1.26 |

of the simulated intercepted snow mass against observations. Overall, the model performs well and similarly to Essery et al. (2003) and Lundquist et al. (2021). Snow tends to remain too long in the trees and SVS2 does not capture abrupt unloading events observed at this site. This limitation can be associated with the exponential decay relationship used in the SVS2 snow unloading scheme (Sect. 2.3.4 in the main manuscript, Mazzotti et al. (2020)). Lundquist et al. (2021) demonstrated that, at

Umpqua, interception schemes in which interception efficiency varies with air temperature—such as the one implemented in SVS2 (Andreadis et al., 2009)—performed better when paired with temperature-wind unloading compared to exponential decay unloading. Future versions of SVS2 will consider representing snow unloading as a function of wind speed (e.g., Roesch et al., 2001). The performance of simulated interception at Umpqua was also very sensitive to phase partitioning of precipitation (not shown).

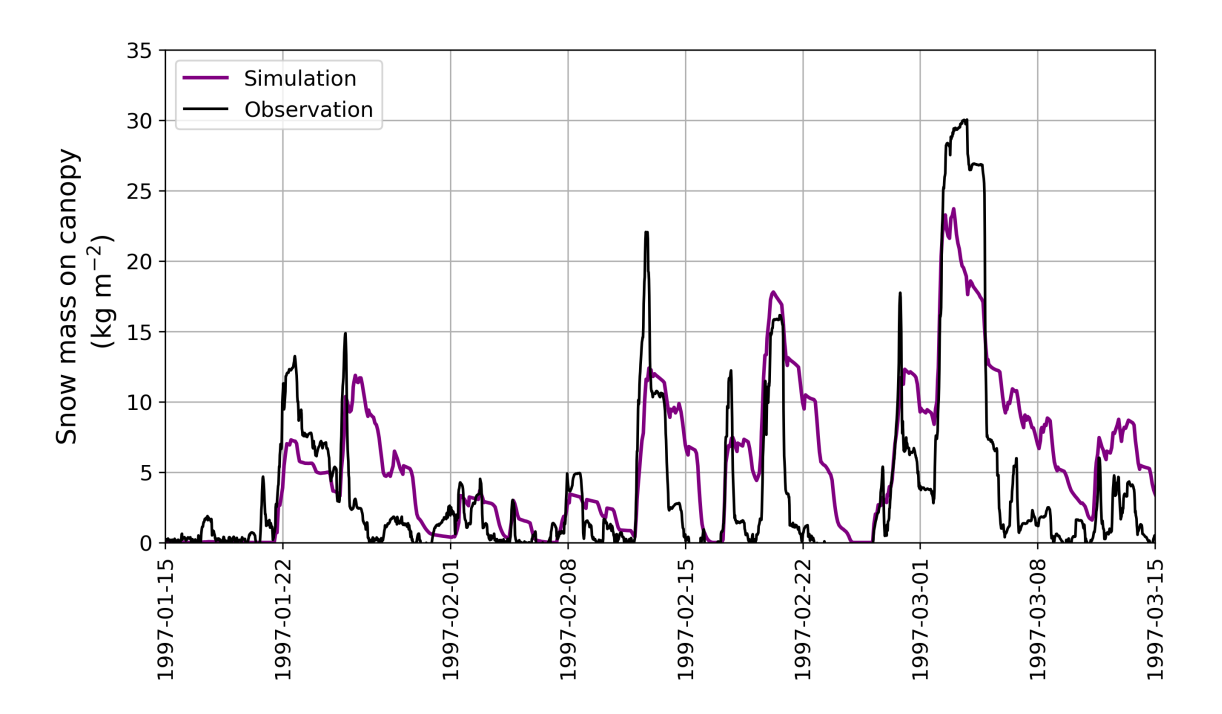


Figure S5. Simulated and observed intercepted snow mass on the canopy in Umpqua, Oregon, USA (Storck et al., 2002).

S4 Distributed snowpack simulations

S4.1 Simulation domain

530

Figure S6a shows the elevation over the simulation domain that extends from southern Quebec to the north of the Canadian Arctic. The spatial distribution over this domain of the snow darkening coefficient for the Crocus albedo parameterization (Gaillard et al., 2024, 2025) is shown on Fig. S6b.

S4.2 Snow melt-out date for winter 2015/16

Figure S7 displays the snow melt-out date (SMOD) map derived from the GMASI product for the 2015/16 winter and compares it against three SVS2/Crocus configurations and two benchmark datasets— *ERA5L* and *ERA5-CRO*. Figure S8 shows how the SMOD in GMASI and different snow products evolves on average with latitude.

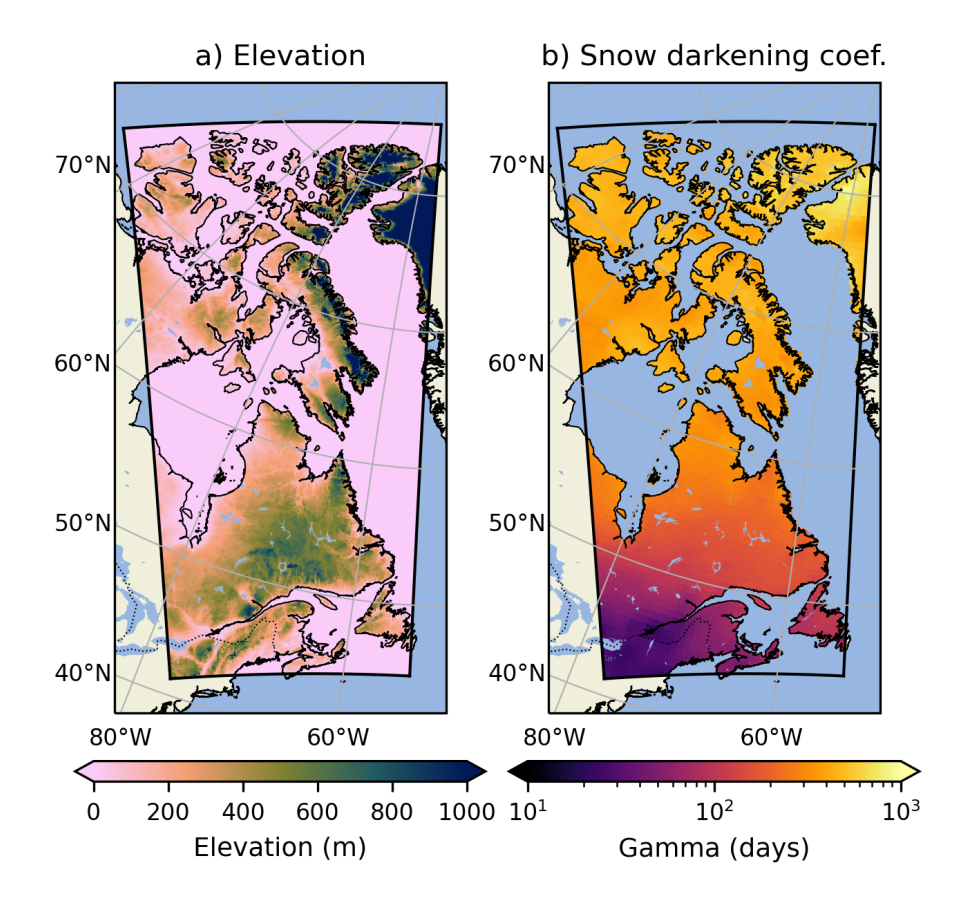


Figure S6. (a) Elevation (m) over the domain of the distributed simulation and (b) optimized snow darkening coefficient taken from Gaillard et al. (2024) over the same domain.

References

545

550

Alavi, N., Bélair, S., Fortin, V., Zhang, S., Husain, S. Z., Carrera, M. L., and Abrahamowicz, M.: Warm season evaluation of soil moisture prediction in the Soil, Vegetation, and Snow (SVS) scheme, J. Hydrometeorol., 17, 2315–2332, https://doi.org/https://doi.org/10.1175/JHM-D-15-0189.1, 2016.

Andreadis, K. M., Storck, P., and Lettenmaier, D. P.: Modeling snow accumulation and ablation processes in forested environments, Water resources research, 45, 2009.

Bartsch, A., Widhalm, B., Leibman, M., Ermokhina, K., Kumpula, T., Skarin, A., Wilcox, E. J., Jones, B. M., Frost, G. V., Höfler, A., et al.: Feasibility of tundra vegetation height retrieval from Sentinel-1 and Sentinel-2 data, Remote Sensing of Environment, 237, 111 515, 2020. Beljaars, A. and Holtslag, A.: Flux parameterization over land surfaces for atmospheric models, J. Appl. Meteorol., 30, 327–341, 1991.

Boone, A. and Etchevers, P.: An intercomparison of three snow schemes of varying complexity coupled to the same land surface model: local-scale evaluation at an Alpine site, J. Hydrometeor., 2, 374–394, 2001.

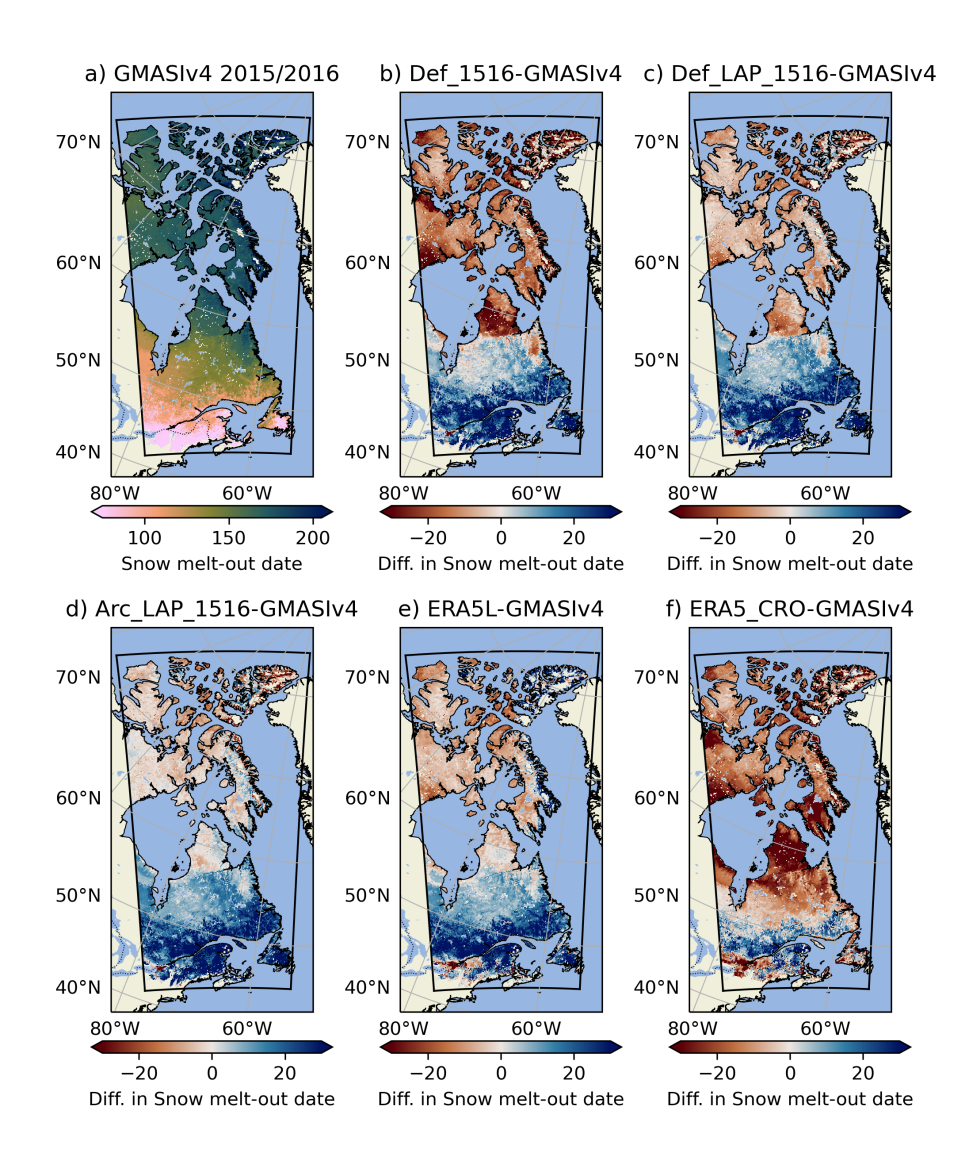


Figure S7. (a) Snow melt-out date derived from the GMASI product for winter 2015/16; (b) Difference of snow melt-out date between the Def configuration of SVS2/Crocus and GMASI; (c) Same as (b) for the Def_{LAP} configuration of SVS2/Crocus, (d) Same as (b) for the ArcW configuration of SVS2/Crocus; (e) Same as (b) for ERA5L and (f) Same as (b) for ERA5CRO.

Boone, A., Masson, V., Meyers, T., and Noilhan, J.: The influence of the inclusion of soil freezing on simulations by a soil-vegetation-atmosphere transfer scheme, J. Appl. Meteorol., 39, 1544–1569, https://doi.org/https://doi.org/10.1175/1520-0450(2000)039<1544:TIOTIO>2.0.CO;2, 2000.

555

Boone, A., Samuelsson, P., Gollvik, S., Napoly, A., Jarlan, L., Brun, E., and Decharme, B.: The interactions between soil-biosphere—atmosphere land surface model with a multi-energy balance (ISBA-MEB) option in SURFEXv8—Part 1: Model description, Geoscientific Model Development, 10, 843–872, 2017.

Statistics for Snow melt-out date for 2015/2016

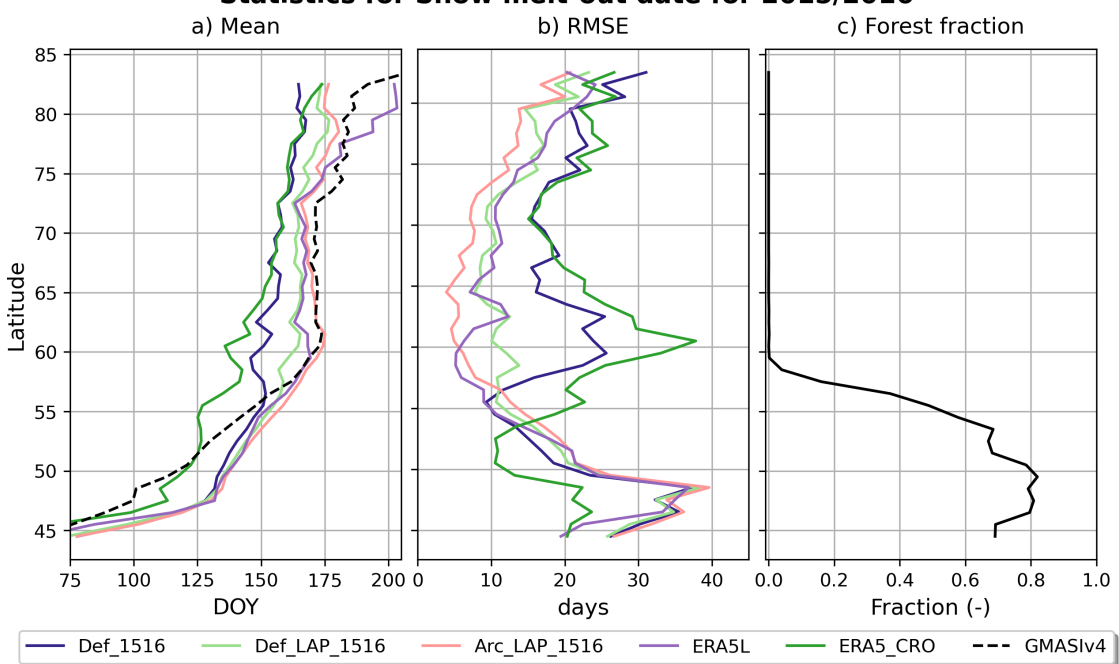


Figure S8. (a) Mean snow melt-out data for winter 2015/16 as a function of latitude for different snow products; (b) Mean RMSE as a function of latitude computed using GMASI as the reference and (c) forest fraction as a function of latitude. Points fully covered by water, lake and/or glaciers were removed from the analysis.

Boussetta, S., Balsamo, G., Arduini, G., Dutra, E., McNorton, J., Choulga, M., Agustí-Panareda, A., Beljaars, A., Wedi, N., Munõz-Sabater, J., et al.: ECLand: The ECMWF land surface modelling system, Atmosphere, 12, 723, 2021.

560

565

Brooks, R. H. and Corey, A. T.: Properties of porous media affecting fluid flow, Journal of the irrigation and drainage division, 92, 61–88, 1966.

Brun, E., Vionnet, V., Boone, A., Decharme, B., Peings, Y., Valette, R., Karbou, F., and Morin, S.: Simulation of northern Eurasian local snow depth, mass, and density using a detailed snowpack model and meteorological reanalyses, Journal of Hydrometeorology, 14, 203–219, 2013.

Decharme, B., Boone, A., Delire, C., and Noilhan, J.: Local evaluation of the Interaction between Soil Biosphere Atmosphere soil multilayer diffusion scheme using four pedotransfer functions, J. Geophys. Res: Atm., 116, 2011.

Decharme, B., Martin, E., and Faroux, S.: Reconciling soil thermal and hydrological lower boundary conditions in land surface models, Journal of Geophysical Research: Atmospheres, 118, 7819–7834, 2013.

570 Decharme, B., Brun, E., Boone, A., Delire, C., Le Moigne, P., and Morin, S.: Impacts of snow and organic soils parameterization on northern Eurasian soil temperature profiles simulated by the ISBA land surface model, The Cryosphere, 10, 853–877, 2016.

Delage, Y. and Girard, C.: Stability functions correct at the free convection limit and consistent for for both the surface and Ekman layers, Boundary-Layer Meteorology, 58, 19–31, 1992.

- Dickinson, R. E.: Modeling evapotranspiration for three-dimensional global climate models, Climate processes and climate sensitivity, 29, 58–72, 1984.
 - Essery, R., Pomeroy, J., Parviainen, J., and Storck, P.: Sublimation of snow from coniferous forests in a climate model, Journal of Climate, 16, 1855–1864, 2003.
 - Fang, X., Pomeroy, J. W., DeBeer, C. M., Harder, P., and Siemens, E.: Hydrometeorological data from Marmot Creek Research Basin, Canadian Rockies, Earth System Science Data, 11, 455–471, 2019.
- Fuchs, M., Campbell, G., and Papendick, R.: An analysis of sensible and latent heat flow in a partially frozen unsaturated soil, Soil Science Society of America Journal, 42, 379–385, 1978.
 - Gaillard, M., Vionnet, V., Lafaysse, M., Dumont, M., and Ginoux, P.: Improved snow darkening coefficient for large-scale albedo modelling with Crocus [Dataset], Zenodo, https://doi.org/10.5281/zenodo.14194990, 2024.
 - Gaillard, M., Vionnet, V., Lafaysse, M., Dumont, M., and Ginoux, P.: Improving large-scale snow albedo modeling using a climatology of light-absorbing particle deposition, The Cryosphere, 19, 769–792, https://doi.org/10.5194/tc-19-769-2025, 2025.
 - Ganji, A., Sushama, L., Verseghy, D., and Harvey, R.: On improving cold region hydrological processes in the Canadian Land Surface Scheme, Theoretical and Applied Climatology, 127, 45–59, 2017.
 - Giard, D. and Bazile, E.: Implementation of a new assimilation scheme for soil and surface variables in a global NWP model, Mon. Wea. Rev., 128, 997–1015, 2000.
- 590 Gouttevin, I., Lehning, M., Jonas, T., Gustafsson, D., and Mölder, M.: A two-layer canopy model with thermal inertia for an improved snowpack energy balance below needleleaf forest (model SNOWPACK, version 3.2. 1, revision 741), Geoscientific Model Development, 8, 2379–2398, 2015.
 - Hansen, M. C., Potapov, P. V., Moore, R., Hancher, M., Turubanova, S. A., Tyukavina, A., Thau, D., Stehman, S. V., Goetz, S. J., Loveland, T. R., et al.: High-resolution global maps of 21st-century forest cover change, science, 342, 850–853, 2013.
- Hansen, M. C., Potapov, P. V., Pickens, A. H., Tyukavina, A., Hernandez-Serna, A., Zalles, V., Turubanova, S., Kommareddy, I., Stehman, S. V., Song, X.-P., et al.: Global land use extent and dispersion within natural land cover using Landsat data, Environmental Research Letters, 17, 034 050, 2022.
 - Harder, P. and Pomeroy, J.: Estimating precipitation phase using a psychrometric energy balance method, Hydrol. Proc., 27, 1901–1914, https://doi.org/https://doi.org/10.1002/hyp.9799, 2013.
- 600 Husain, S. Z., Alavi, N., Bélair, S., Carrera, M., Zhang, S., Fortin, V., Abrahamowicz, M., and Gauthier, N.: The multibudget Soil, Vegetation, and Snow (SVS) scheme for land surface parameterization: Offline warm season evaluation, J Hydrometeorol., 17, 2293–2313, https://doi.org/https://doi.org/10.1175/JHM-D-15-0228.1, 2016.
 - Johansen, O.: Thermal conductivity of soils, Ph.D. thesis, University of Trondheim, 1975.

- Koivusalo, H. and Kokkonen, T.: Snow processes in a forest clearing and in a coniferous forest, Journal of Hydrology, 262, 145-164, 2002.
- Kurylyk, B. L. and Watanabe, K.: The mathematical representation of freezing and thawing processes in variably-saturated, non-deformable soils, Advances in Water Resources, 60, 160–177, 2013.
 - Lafaysse, M., Cluzet, B., Dumont, M., Lejeune, Y., Vionnet, V., and Morin, S.: A multiphysical ensemble system of numerical snow modelling, The Cryosphere, 11, 1173–1198, https://doi.org/https://doi.org/10.5194/tc-11-1173-2017, 2017.
 - Lawrence, D. M. and Slater, A. G.: Incorporating organic soil into a global climate model, Climate Dynamics, 30, 145-160, 2008.

610 Lundquist, J. D., Dickerson-Lange, S., Gutmann, E., Jonas, T., Lumbrazo, C., and Reynolds, D.: Snow interception modelling: Isolated observations have led to many land surface models lacking appropriate temperature sensitivities, Hydrological processes, 35, e14 274, 2021.

- Martynov, A., Laprise, R., Sushama, L., Winger, K., Šeparović, L., and Dugas, B.: Reanalysis-driven climate simulation over CORDEX North America domain using the Canadian Regional Climate Model, version 5: model performance evaluation, Climate Dynamics, 41, 2973–3005, 2013.
- Mazzotti, G., Essery, R., Moeser, C. D., and Jonas, T.: Resolving small-scale forest snow patterns using an energy balance snow model with a one-layer canopy, Water Resources Research, 56, e2019WR026 129, 2020.
- Monteiro, D., Caillaud, C., Lafaysse, M., Napoly, A., Fructus, M., Alias, A., and Morin, S.: Improvements in the land surface configuration to better simulate seasonal snow cover in the European Alps with the CNRM-AROME (cycle 46) convection-permitting regional climate model, Geoscientific Model Development, 17, 7645–7677, 2024.
 - Musselman, K. N., Pomeroy, J. W., and Link, T. E.: Variability in shortwave irradiance caused by forest gaps: Measurements, modelling, and implications for snow energetics, Agricultural and Forest Meteorology, 207, 69–82, https://doi.org/https://doi.org/10.1016/j.agrformet.2015.03.014, 2015.
- Napoly, A., Boone, A., Samuelsson, P., Gollvik, S., Martin, E., Seferian, R., Carrer, D., Decharme, B., and Jarlan, L.: The interactions between soil-biosphere-atmosphere (ISBA) land surface model multi-energy balance (MEB) option in SURFEXv8-Part 2: Introduction of a litter formulation and model evaluation for local-scale forest sites, Geoscientific Model Development, 10, 1621–1644, 2017.
 - Niu, G.-Y. and Yang, Z.-L.: Effects of frozen soil on snowmelt runoff and soil water storage at a continental scale, Journal of Hydrometeorology, 7, 937–952, 2006.
- Noilhan, J. and Planton, S.: A simple parameterization of land surfaces processes for meteorological models, Mon. Wea. Rev., 117, 536–549, 1989.
 - Noilhan, J., , and Lacarrere, P.: GCM grid-scale evaporation from mesoscale modeling, Journal of climate, 8, 206-223, 1995.
 - Peters-Lidard, C., Blackburn, E., Liang, X., and Wood, E. F.: The effect of soil thermal conductivity parameterization on surface energy fluxes and temperatures, Journal of the Atmospheric Sciences, 55, 1209–1224, 1998.
- Poggio, L., De Sousa, L. M., Batjes, N. H., Heuvelink, G. B., Kempen, B., Ribeiro, E., and Rossiter, D.: SoilGrids 2.0: producing soil information for the globe with quantified spatial uncertainty, Soil, 7, 217–240, 2021.
 - Pomeroy, J., Parviainen, J., Hedstrom, N., and Gray, D.: Coupled modelling of forest snow interception and sublimation, Hydrological processes, 12, 2317–2337, 1998.
 - Pomeroy, J. W. and Schmidt, R.: The use of fractal geometry in modelling intercepted snow accumulation and sublimation, in: Proceedings of the Eastern Snow Conference, vol. 50, pp. 1–10, 1993.
- Raynolds, M. K., Walker, D. A., Balser, A., Bay, C., Campbell, M., Cherosov, M. M., Daniëls, F. J., Eidesen, P. B., Ermokhina, K. A., Frost, G. V., et al.: A raster version of the Circumpolar Arctic Vegetation Map (CAVM), Remote Sensing of Environment, 232, 111 297, 2019.
 - Roesch, A., Wild, M., Gilgen, H., and Ohmura, A.: A new snow cover fraction parametrization for the ECHAM4 GCM, Climate Dynamics, 17, 933–946, 2001.
- Royer, A., Picard, G., Vargel, C., Langlois, A., Gouttevin, I., and Dumont, M.: Improved simulation of arctic circumpolar land area snow properties and soil temperatures, Frontiers in Earth Science, 9, 685 140, 2021.
 - Schenk, H. J. and Jackson, R. B.: Mapping the global distribution of deep roots in relation to climate and soil characteristics, Geoderma, 126, 129–140, 2005.

- Shangguan, W., Dai, Y., Duan, Q., Liu, B., and Yuan, H.: A global soil data set for earth system modeling, J. Adv. Model. Earth Sy., 6, 249–263, https://doi.org/10.1002/2013MS000293, 2014.
- Soulis, E., Craig, J., Fortin, V., and Liu, G.: A simple expression for the bulk field capacity of a sloping soil horizon, Hydrological Processes, 25, 112–116, 2011.
 - Storck, P., Lettenmaier, D. P., and Bolton, S. M.: Measurement of snow interception and canopy effects on snow accumulation and melt in a mountainous maritime climate, Oregon, United States, Water resources research, 38, 5–1, 2002.
 - Sumner, M. E.: Handbook of soil science, CRC press, 1999.

- Trigo, I., Boussetta, S., Viterbo, P., Balsamo, G., Beljaars, A., and Sandu, I.: Comparison of model land skin temperature with remotely sensed estimates and assessment of surface-atmosphere coupling, Journal of Geophysical Research: Atmospheres, 120, 12–096, 2015.
 - Vionnet, V., Brun, E., Morin, S., Boone, A., Faroux, S., Le Moigne, P., Martin, E., and Willemet, J.-M.: The detailed snowpack scheme Crocus and its implementation in SURFEX v7.2, Geosci. Model. Dev., 5, 773–791, https://doi.org/10.5194/gmd-5-773-2012, 2012.
 - Wang, Y.-H., Broxton, P., Fang, Y., Behrangi, A., Barlage, M., Zeng, X., and Niu, G.-Y.: A wet-bulb temperature-based rain-snow partitioning scheme improves snowpack prediction over the drier western United States, Geophys. Res. Lett., 46, 13825–13835, https://doi.org/10.1029/2019GL085722, 2019.
 - Woolley, G. J., Rutter, N., Wake, L., Vionnet, V., Derksen, C., Essery, R., Marsh, P., Tutton, R., Walker, B., Lafaysse, M., and Pritchard, D.: Multi-physics ensemble modelling of Arctic tundra snowpack properties, EGUsphere, 2024, 1–37, 2024.
- Zhao, L., Gray, D. M., and Male, D. H.: Numerical analysis of simultaneous heat and mass transfer during infiltration into frozen ground,

 Journal of Hydrology, 200, 345–363, 1997.